X 86-10375

X 86-10375 #

NASA Technical Memorandum 87030

Wind-Tunnel Results of Advanced High-Speed Propellers at Takeoff, Climb, and Landing Mach Numbers

George L. Stefko and Robert J. Jeracki
Lewis Research Center
Cleveland, Ohio

November 1985

NASA

WIND-TUNNEL RESULTS OF ADVANCED HIGH-SPEED PROPELLERS AT

TAKEOFF, CLIMB, AND LANDING MACH NUMBERS

George L. Stefko and Robert J. Jeracki
National Aeronautics and Space Administration
Lewis Research Center
Cleveland, Ohio 44135

SUMMARY

Low-speed wind-tunnel performance tests of two advanced propellers have been completed at the NASA Lewis Research Center as part of the NASA Advanced Turboprop Program. The 62.2-cm- (24.5 in-) diameter adjustable-pitch models were tested at Mach numbers from 0.10 to 0.34 at zero angle of attack in the Lewis 10- by 10-Foot Supersonic Wind Tunnel to establish the performance of the two propeller models in the takeoff, initial climbout, and landing speed regimes. Previous tests had concentrated on measuring the performance of these propellers at the higher Mach numbers of 0.60 to 0.85.

Both models had eight blades and a cruise-design-point operating condition of Mach 0.80, a 10.668-km (35 000-ft) I.S.A. altitude, a 243.8-m/s (800-ft/sec) tip speed, and a high-power loading of 301 kW/m^2 (37.5 shp/ft^2). The straight-blade model (SR-2) was tested with an integrally designed area-ruled spinner and specially contoured nacelle. The 45°-swept-blade model (SR-3) was tested with a different area-ruled spinner and the same contoured nacelle. The 45° blade sweep was incorporated to minimize high Mach number performance losses and to produce acoustical phase interference which would reduce noise levels. The spinner and nacelle contours were selected to reduce blade-section Mach numbers and to relieve blade-root choking.

No adverse or unusual low-speed operating conditions were found during the test with either the straight-blade SR-2 or the 45°-swept SR-3 propeller. At a takeoff condition of Mach 0.20, an advance ratio of 0.875, and a power coefficient of 1.00, the net efficiencies of the straight and 45°-swept propellers were 50.2 and 54.9 percent, respectively. At a climb condition of Mach 0.34, an advance ratio of 1.40, and a power coefficient of 1.70, the net efficiencies of the straight and 45°-swept propellers were 53.7 and 59.1 percent, respectively.

INTRODUCTION

The attractiveness of advanced turboprop propulsion results from its potential for very high efficiency at cruise speeds up to Mach 0.8. Figure 1 compares the installed cruise efficiency of turboprop-powered and turbofan-powered propulsive systems over a range of cruise speeds. The efficiencies shown include the installation losses for both systems, namely, nacelle drag for the turboprop systems and fan-cowling external drag and internal-fan air-flow losses associated with inlet recovery and nozzle efficiency for the turbofan systems. Conventional lower speed turboprops, such as the Electra, have installed efficiencies above 80 percent at speeds up to about Mach 0.5, but can suffer from rapid decreases in efficiency above this speed because of increasing propeller-compressibility losses. These losses are primarily the

result of relatively thick blades (5 to 7 percent of chord at 75-percent radius) used on many propeller propulsion systems operating at high helical-tip Mach numbers.

The advanced high-speed turboprop has the potential to delay these compressibility losses to a much higher cruise speed and achieve a relatively high performance to at least Mach 0.8 cruise. Although high-bypass-ratio turbofans exhibit their highest efficiency at cruise speeds near Mach 0.8, their performance would still be significantly below that of the advanced turboprops.

A number of studies have been conducted by both NASA and industry to evaluate the potential of advanced high-speed turboprop propulsion for both civil and military applications. Numerous references to specific studies and summary results are listed in reference 1. Installed efficiencies (similar to those shown in fig. 1) for comparable-technology advanced turboprops and turbofans were used in most of these studies. At Mach 0.8, the installed efficiency of the turbofan system would be about 65 percent, while the installed efficiency of the advanced turboprop would be about 75 percent. At lower cruise speeds, the efficiency advantage of the advanced turboprop would be even larger.

Figure 2, which shows block fuel savings as a function of trip-stage length, is a summary of the reference 1 studies. As shown in figure 2, block fuel savings depends on aircraft cruise speed and range. At Mach 0.8 cruise (which is represented by the bottom of the band), fuel savings range from about 15 to 25 percent for advanced turboprop aircraft when compared to equivalent-technology turbofan aircraft. The larger fuel savings occur at the shorter operating ranges, where the mission is climb and descent dominated. Because of the lower operating speeds encountered during climb and descent, turboprops have an even larger performance advantage over the turbofans than they do during Mach 0.8 cruise. In a similar manner, a larger fuel savings is possible at Mach 0.7 cruise (which is represented by the top of the band in fig. 2). At this lower cruise speed, fuel savings range from about 20 percent to near 30 percent. Even larger fuel savings may be possible by recovering the propeller swirl loss from these single-rotation turboprops. Swirl-recovery vanes and counter-rotation are two promising concepts for recovering the swirl loss. In addition, advanced airfoils can also improve perfomance. All these concepts are currently under study at NASA Lewis and in the industry.

In view of the attractive fuel-savings potential of the advanced high-speed turboprop propulsion system, NASA Lewis has established the Advanced Turboprop Program. This major research and technology program (ref. 2) establishes the technology base required to lead to the application of the advanced turboprop-propulsion-system concept. One phase of this overall program was to establish the low-speed aerodynamic performance of the SR-2 and SR-3 propeller models in the takeoff, initial climbout, and landing speed regimes. The first model (shown mounted in the wind tunnel in fig. 3) had straight blades, while the second model (fig. 4) had 45° of blade sweep for lower noise and improved propeller efficiency. Both propeller models were tested in the NASA Lewis 10- by 10-Foot Supersonic Wind Tunnel on the Lewis propeller test rig. This report presents the detailed wind-tunnel test results of the two propellers in the takeoff, climb, and landing speed regimes (Mach 0.10 to 0.34). A summary of this report can be found in reference 3. Previous wind-tunnel tests have measured the performance of these propellers primarily in the higher speed regime of Mach 0.60 to 0.85 (refs. 1 and 4).

2

AERODYNAMIC DESIGN CONCEPTS AND MODEL DESCRIPTION

To achieve the previously described fuel savings, the propeller on the advanced turboprop would have to incorporate a number of unique design features that would enhance propeller performance and lower source noise. These unique design features are required to reduce blade-compressibility losses and attain high efficiency in the transonic Mach number regime. A propeller designed for a cruise Mach number of 0.80 at an altitude above 9.144 km (30 000 ft) would have local blade Mach numbers from just over 0.8 at the blade hub to supersonic (near 1.15) at the blade tip. The inherent detrimental effects of these high Mach numbers on performance are negated by the design concepts shown in figure 5. These concepts include proper shaping of the nacelle to reduce inboard-blade Mach number, blade sweep to reduce outboard-blade local Mach number, thinner blades to increase drag-rise Mach number, and spinner area ruling to prevent inboard blade choking. To hold propeller diameter to a reasonable value, a high power (or disk) loading, and concomitantly, a large number of blades (eight or ten) and increased chord length are required. The inboard portion of the propeller then operates as a cascade rather than as isolated blades. These design concepts are incorporated in the two model propellers that are described in more detail in this report.

The propeller models (figs. 3 and 4) were both designed for an operating condition of Mach 0.80, a 10.668-km (35 000-ft) I.S.A. altitude, a 243.8-m/s (800-ft/sec) tip speed, and a power loading of 301 kW/m^2 (37.5 shp/ft^2). Both models have a diameter of 0.622 m (24.5 in.), which was determined by the design power loading. The overall design characteristics and planforms of the two models are presented in table I.

The aerodynamic, conic-corrected, blade-shape characteristics that are along the mean flow streamlines are presented for the SR-2 propeller in figure 6 and for the 45°-swept SR-3 propeller in figure 7. The thickness ratio t/b, twist $\Delta\beta$, design lift coefficient C_{LD}, and planform b/D distribution were established to provide a loading distribution at the design condition for high efficiency, and for the SR-3 propeller, low noise as well. (All symbols are also defined in appendix A.)

The airfoil sections selected for the SR-2 and SR-3 blade design are NACA Series 16, from the tip to the 45- and 53-percent radius, respectively, and NACA Series 65 with circular arc (CA) camber lines, from the 37-percent radius to the root (with a transition fairing between them). These airfoils were chosen for their high critical Mach numbers and their wide, low-drag buckets.

The area-ruled spinners and nacelle lines (table II) are designed to alleviate blade-root choking and minimize compressibility drag rise. The spinners incorporate area ruling and blend into the nacelle. The nacelle has a maximum diameter equal to 35 percent of the model propeller diameter.

The reference diameter D_{ref} of 62.2 cm (24.5 in.) was the same for both models. The diameter of the straight-blade SR-2 propeller changed negligibly as blade angle or tip speed was varied. The diameter of the variable-pitch propeller with swept blades changed slightly as the blade angle and rotational speed were varied, as shown in figure 8. This small change occurred because the blade tip traveled out of the axial-radial plane and, as such, was not equivalent to a true radial-diameter increase. Therefore, the reference diameter D_{ref} of 0.622 m (24.5 in.) was selected to define the reference

3

lower coefficient C_P, thrust coefficient $C_{T,ref}$, and advance ratio J_{ref} used in the basic performance maps.

The performance data were acquired for a model configuration which had the gaps between the propeller blade roots and the hub surface sealed. The gaps were disproportionately large for the model and were sealed to be more representative of a full-scale propeller. (More design information may be found in refs. 1, 4 and 5.)

TEST FACILITIES

Wind Tunnel

The SR-2 and SR-3 propeller model tests were conducted in the NASA Lewis 10- by 10-Foot Supersonic Wind Tunnel. This tunnel (ref. 6) incorporates a 13.12-m- (40-ft-) long, solid-wall test section. Nominal test-section Mach numbers can vary subsonically from 0.10 to 0.34 and supersonically from 2.0 to 3.5. For this test program, the tunnel was run in the aerodynamic cycle rather than the propulsion cycle. During the aerodynamic cycle, the tunnel is operated as a closed system with makeup air added only as required to maintain the desired tunnel conditions. The free-stream velocity corrections due to the propeller thrust in this solid-wall tunnel are discussed in detail in appendix B.

Propeller Test Rig

The 746-kW (1000-hp) propeller test rig (PTR) was designed and developed specifically for conducting research on advanced propellers in the Lewis 10- by 10-ft and 8- by 6-ft wind tunnels. The PTR was strut-mounted from the ceiling in the tunnel test section. Figure 4 shows the PTR and the SR-3 model in the tunnel, and a cutaway view of the PTR is presented in figure 9. The model is driven by a three-stage air turbine using high-pressure (3.1×10^6-N/m^2 (450-psi)) air which is heated to 367 K (660 °R). The turbine is capable of delivering nearly 746 kW (1000 hp) to the propeller model.

The PTR force measuring system includes two separate axial-force measuring systems. The primary system is a rotating balance which measures the thrust and torque of the propeller and spinner. The second system includes a load cell located in the vertical strut. When corrected for internal forces, both systems measure only propeller blade and spinner forces. Model parts (other than the spinner and blades) that are being measured by the strut-mounted load cell are shielded from the free-stream tunnel air by a windscreen (fig. 9).

Extensive static calibrations of the load cell and rotating balance were done. The load cell was calibrated statically for thrust in the -890 to 3559 N (-200 to +800 lbf) operating range. The rotating balance was also calibrated statically for thrust, -1557 to 3559 N (-350 to 800 lbf) and torque, 0 to 813 J (0 to 600 ft-lbf).

Two dynamic calibrations of the rotating balance were done. The first .calibration was performed with only the spinner installed, and it measured the effect of rotational speed on the thrust and torque output of the rotating balance. The second calibration was performed with the propeller blades

installed, and it measured the effect of rotational speed on the thrust output of the rotating balance.

Both static and dynamic calibrations were repeated several times. Moreover, the calibrations were performed before, during, and after the tests to assure that no changes occurred during the tests.

Pressure Instrumentation

A total of 165 PTR pressures and 31 tunnel pressures were measured and digitized with a measurement system which used individual transducers for each pressure measurement. Some pressure measurements were made inside the PTR (table III and fig. 10). These measurements were necessary to obtain the propeller apparent thrust from the balance axial-force measurements. Other pressure measurements were made on the surface of the nacelle. These measurements incorporated four azimuthal rows of static-pressure taps at the coordinates listed in table III. Nacelle pressures were measured for each test performance point and for special tare runs. The tare runs were made with a special spinner which had no blade holes. These measurements were used to obtain an incremental nacelle-pressure force and, with the apparent thrust values, provided the required net thrust values for the model propeller. These testing procedures are discussed in more detail in the next section and in appendix C.

As well as acquiring and digitizing the balance and pressure data, about 20 temperatures were measured with thermocouples and digitized using the Lewis data system. Then, all of these digitized data were sent to the Escort II data-acquisition system which recorded the data. Finally, the data were sent to the IBM-370 computer to calculate the desired parameters. Rotational speed, torque, and measurements of axial force were filtered before they were recorded. All of the reduced wind-tunnel and PTR data were available in about 7 sec.

PROPELLER NET FORCE MEASUREMENTS

The net propeller thrust is defined as the propulsive force of the blades operating in the presence of the spinner and nacelle flow field without the increase in thrust (i.e., apparent thrust) due to the mutual interaction among the propeller blades, the spinner, and the nacelle.

To determine the difference between apparent and net thrust, model tare tests were made first without the propeller blades to evaluate both the external-spinner aerodynamic drag and the nacelle-pressure drag.

In these tare tests, the spinner was replaced by a dummy hub having no holes for the blades. A special series of experimental runs was made without the blades to define the spinner aerodynamic and nacelle-pressure drag for the same range of tunnel Mach numbers as would be tested with the model blades. As shown in figure 11, the spinner drag D_{ST} was measured directly from the force balance and was corrected for the internal-pressure area forces. The nacelle-pressure drag D_{NT} was determined by pressure integration of the longitudinal rows of area-weighted pressure orifices. Spinner aerodynamic drag and nacelle-pressure drag coefficients obtained in these tare tests are shown in figures 12 and 13.

5

With the blades installed and thrusting, the force balance measures the algebraic sum of the propeller thrust, the spinner drag, and the internal-pressure area forces. The model forces are as shown in figure 14. The uncorrected propeller thrust T_{prop} (fig. 14) is defined as follows:

$$T_{prop} = FB - \sum PA_{int} + D_S$$

When this uncorrected propeller thrust is corrected for the change in spinner drag ΔD_S between the powered data (fig. 14) and the tare data (fig. 11),

$$\Delta D_S = D_S - D_{ST}$$

the apparent thrust of the propeller is obtained from

$$T_{app} = T_{prop} - \Delta D_S$$

or

$$T_{app} = FB - \sum PA_{int} + D_{ST}$$

where $PA_{int} = (p - p_0) A_{int}$. Next the nacelle pressure drag is obtained from nacelle surface pressure integrations:

$$D_N = \int (p - p_0) \, dA$$

Then the change in nacelle pressure drag, ΔD_N, is obtained from the difference between these and the tare run pressure integrations:

$$\Delta D_N = D_N - D_{NT}$$

And finally, the net thrust is obtained by subtracting the change in nacelle-pressure drag from the apparent thrust:

$$T_{net} = T_{app} - \Delta D_N$$

TEST DESCRIPTION

The SR-2 and SR-3 propeller models were tested at zero angle of attack over a range of Mach numbers from 0.10 to 0.34 and blade angles from 24.6° to 62.1°. The blade angle measured at 75 percent of the propeller radius $\beta_{0.75R}$ becomes 90° when the chord of that airfoil section is aligned directly with the flight direction. At each blade angle, model thrust and power were measured over a range of Mach numbers and rotational speeds. The blade-angle/Mach number combinations tested are listed in table IV for the SR-2 propeller and in table V for the SR-3 propeller. At each blade-angle/Mach number combination, measurements were taken over an rpm range from the windmilling value to 9000 rpm (the maximum rpm allowed by blade-stress limitations). Each rotational speed setting constituted a test point.

A special test procedure was adopted based on using measurements from both the rotating balance and the strut-mounted load cell shown in figure 9. This procedure was required to overcome a slow thermal drift in the thrust reading of the rotating balance, which was apparently due to heat generated by its bearings. An initial series of wind-tunnel runs was made to establish

6

reference windmill drags for each blade-angle/Mach number combination by using the strut-mounted force system. During this testing, to minimize any errors due to tunnel air passing over the metric parts of the model, a cover plate was installed on the aft end of the model. After the reference windmill drags were established, incremental thrust data were obtained by using the rotating balance in a windmill-power-windmill test sequence. At each desired power point, the model was first windmilled, a power point was taken, and then a second windmill point was taken. An incremental propeller thrust which minimized any thermal drift errors was obtained by subtracting the average of the two rotating-balance windmill points from the thrust at the power point. Incremental thrusts thus determined were added to the reference windmill drags which were determined in the earlier tests with the strut-mounted force system to establish the final thrust values for each power point. This procedure was repeated for each blade-angle/Mach number combination. Torque was determined directly from the rotating balance as it was not sensitive to thermal effects.

A further explanation of this procedure, along with the equations used, is given in appendix C. A direct comparison of propeller performance using this procedure, with measurements from another propeller test rig in a second wind tunnel (ref. 7) is also shown in appendix C. The agreement is good.

RESULTS

Takeoff, Climb, and Landing Performance

The SR-2 and SR-3 experimental data for free-stream Mach numbers of 0.10, 0.20, 0.27, and 0.34 are presented in figures 15 to 38. A group of three performance figures are shown for each test Mach number. The first figure in each group summarizes the propeller performance. It is a propeller performance map which presents the propeller net efficiency η_{net} and reference power coefficient $C_{P,ref}$ for a given Mach number and advance ratio J_{ref} and blade angle. The second figure of the group shows the propeller net efficiency η_{net} as a function of the reference advance ratio J_{ref} for the same blade angles. And, the third figure of the group illustrates the reference power coefficient $C_{P,ref}$ as a function of the reference advance ratio J_{ref} for the same blade angles.

During the testing, no abnormal propeller behavior was encountered. The data for both the SR-2 and the SR-3 propeller were normal except for some blade-angle to blade-angle variability in the peak efficiency.

The variability in peak efficiency was caused by the inability of the large 4448 N (1000-lbf) PTR balance to accurately measure the small thrust forces which exist at peak-propeller-efficiency conditions. For example, a typical thrust of 89 N (20 lbf) at peak efficiency requires 0.89 N (0.2-lbf) accuracy from the 4448 N (1000-lbf) PTR balance to obtain a 1-percent accuracy in efficiency. At practical operating conditions, the propeller thrust levels are in the 890- to 2669-N (200- to 600-lbf) range, and thus, the variability problem with extremely low thrust does not exist.

Other experimental data obtained by Hamilton Standard at Mach 0.20 in the United Technologies Research Center tunnel were available for comparison with the data presented in this report. These comparisons for the SR-2 and SR-3 propellers are shown in figures 39 to 42. In these figures, the data compare

7

well, as is illustrated in the following specific comparisons, where linear interpolations of blade angles were used to make the comparison. At the takeoff advance ratio of 0.875 and a power coefficient of 1.00, the measured SR-2 propeller net efficiency was 50.2 percent at Lewis compared with 49.7 percent at Hamilton Standard. Similarly, the measured SR-3 takeoff propeller net efficiency was 54.9 percent at Lewis compared with 54.2 percent at Hamilton Standard. The data agreement is good, especially when one considers that the data were acquired with two different propeller test rigs, two different test techniques, and two different wind tunnels.

From the data presented in figures 15 to 38, the performance of the straight-blade SR-2 propeller can be compared with that of the 45°-swept SR-3 propeller at four low-speed operating conditions.

When an airplane is accelerating down the runway, a representative condition would be a Mach number of 0.10, an advance ratio of 0.438, and a power coefficient of 0.50. At this condition, the 45°-swept SR-3 propeller design has an efficiency of 43.5 percent, compared with 38.6 percent for the straight SR-2 propeller design, a 4.9-percent advantage.

Near lift-off, the Mach number would be approximately 0.20, the advance ratio 0.875, and the power coefficient 1.00. At this condition, the swept SR-3 propeller has a net efficiency of 54.9 percent compared with 50.2 percent for the SR-2 propeller, a 4.7-percent advantage.

When the airplane is starting its initial climbout, a typical operating condition would be a Mach number of 0.27, an advance ratio of 1.16, and a power coefficient of 1.37. Again, the 45°-swept SR-3 propeller net efficiency is significantly higher than the SR-2 propeller net efficiency with a value of 57.2 compared with 52.9 percent, a 4.3-percent advantage.

And, finally, when the airplane is farther into its climbout, a representative condition would be a Mach number of 0.34, an advance ratio of 1.40, and a power coefficient of 1.70. At this condition, the 45°-swept SR-3 propeller net efficiency is 59.1 percent, compared with 53.7 percent for the straight SR-2 propeller, a 5.4-percent advantage.

Thus, the measured data show that in the low-speed operating regime, the 45°-swept SR-3 propeller net efficiency exceeded the net efficiency of the straight-blade SR-2 propeller by about 4 to 5 percent. The SR-3 performance improvement over the SR-2 performance was due to a higher design lift distribution C_{LD} and a higher activity factor AF. Both of these factors allowed the propeller airfoils to absorb a given amount of power at a lower angle of attack and, thus, at a higher lift-to-drag ratio.

Reverse Thrust

In view of the importance of reverse-thrust capability of the propulsion system on transport aircraft, the reverse-thrust characteristics of the 45° swept SR-3 propeller were investigated at Mach 0.10 and 0.20. The blade angle was set at -6.8°. Because of mechanical interference, this reverse blade angle was the maximum that could be achieved with the model. The test results are presented in figures 43 and 44 in terms of power and thrust coefficients as a function of advance ratio. In figure 45, the reverse thrust is divided

8

by the takeoff thrust at Mach 0.20. This parameter is presented as a function of velocity for the windmilling and the powered SR-3 propeller. For reference, a curve for a typical turbofan engine is also shown in this figure. The curves show that both the windmilling and the powered SR-3 propeller produce more reverse thrust than that of a typical turbofan engine at Mach 0.20. Thus, the advanced SR-3 eight-blade propeller is capable of producing the large breaking forces desired for transport airplanes.

SUMMARY OF RESULTS

Two adjustable-pitch advanced turboprop-propeller models (the straight-blade SR-2 and the 45°-swept SR-3) were installed in the NASA Lewis 10- by 10-Foot Supersonic Wind Tunnel and were performance tested at subsonic conditions (Mach 0.10 to 0.34) corresponding to typical takeoff, initial climbout, and landing speeds. The following results were obtained:

1. No abnormal low-speed (Mach 0.10 to 0.34) operating problems were found with either the straight-blade SR-2 or the 45°-swept SR-3 propellers.

2. The 45°-swept propeller was more efficient than the straight-blade SR-2 propeller at all low-speed operating conditions. The 45° SR-3 swept-propeller net efficiency exceeded the efficiency of the straight-blade SR-2 propeller by about 4 to 5 percent. Two of the low-speed operating conditions are summarized below:

(a) At the Mach 0.20 takeoff lift-off condition (advance ratio $J = 0.875$ and power coefficient $C_p = 1.0$), the straight-blade SR-2 propeller had a net efficiency of 50.2 percent, while the 45°-swept SR-3 propeller had a net efficiency of 54.9 percent. The swept SR-3 advantage was 4.7 percent.

(b) At the Mach 0.34 climbout condition ($J = 1.40$ and $C_p = 1.70$), the straight-blade SR-2 propeller had a net efficiency of 53.7 percent, while the 45°-swept SR-3 propeller had a net efficiency of 59.1 percent. The swept SR-3 advantage was 5.4 percent.

3. The large amount of reverse thrust measured for the SR-3 propeller indicates that these new propellers are capable of producing more reverse thrust than that of a typical transport turbofan engine at Mach 0.20.

APPENDIX A – SYMBOLS

A   area

AF   blade activity factor, $6250 \int_{r/R \text{ at hub}}^{1.0} (b/D)(r/R)^3 \, d(r/R)$

A_N maximum nacelle area, 383.527 cm^2 (59.447 in.^2)

b   elemental blade chord, m

CA   circular arc

C_{LD} blade design lift coefficient

C_{Li} integrated design lift coefficient, $4 \int_{r/R \text{ at hub}}^{1.0} C_{LD} (r/R)^3 \, d(r/R)$

C_P power coefficient, $P/\rho_0 n^3 D^5$

C_T thrust coefficient, $T/\rho_0 n^2 D^4$

D   propeller diameter, m

D_N nacelle drag, N

D_{NT} nacelle tare drag, N

D_S spinner drag, N

D_{ST} spinner tare force, N

dA   elemental area, m^2

FB   force balance, N

J   advance ratio, V_0/nD

M   Mach number

n   rotational speed, rps

P   power, W

PA   pressure forces, $(p - p_0) \times \text{Area}$, N

p   pressure, N/cm^2

q   dynamic pressure, N/cm^2

R   propeller radius, m

R_N nacelle maximum radius, 11.05 cm (4.35 in.)

r   radius, m

r/R   fractional radius

T   thrust, N

T_{prop} uncorrected propeller thrust, N

t   elemental blade maximum thickness, m

V   velocity, m/sec

X   axial distance, m

XW   axial distance from the propeller plane, m

β blade angle, deg

$\Delta\beta$ change in blade angle from angle at 75 percent of blade radius, deg

$\beta_{0.75R}$ static propeller blade angle at 75 percent of blade radius, deg

η efficiency, $(TV_0/P) \times 100$, percent

ρ mass density, kg/m^3

Subscripts:

app   apparent

int   internal

N   nacelle

o   tunnel free-stream condition

ref   reference, based on 62.2-cm (24.5-in.) reference diameter

s   static

T   tare

W   windmill

APPENDIX B - FREE-STREAM VELOCITY CORRECTION DUE TO PROPELLER THRUST

IN SOLID-WALL 10- BY 10-FOOT SUPERSONIC WIND TUNNEL

The increased velocity in the wake of a thrusting propeller in a solid-wall tunnel causes a reduced velocity and increased static pressure in the free-stream flow surrounding the wake of the propeller. Therefore, the thrust, effective velocity, and advance ratio of the propeller are altered. Pressures were measured on the wind-tunnel wall in order to evaluate the proper velocity correction that was required for this propeller installation. Data were recorded at free-stream Mach numbers of 0.117 and 0.223. At Mach 0.348, no pressure changes due to the thrusting propeller were measured at the wall static-pressure taps. At each Mach number, data were recorded with the propeller at windmill (no power) and at various power (and thrust) levels ranging downward from model limits to the limits of measuring the wall-pressure changes.

Static-pressure tubes were attached to the wind-tunnel wall in order to measure local static-pressure changes as the propeller thrust was increased. The locations of the pressure measurements are shown in figure 46. The pressures were measured by using a single, accurate (6.89 N/m^2 (0.001 psi)), differential pressure transducer. The reference pressure for all differential measurements was a static-pressure tap located far upstream of the propeller. Figure 46 also identifies the location of a ceiling static pressure labeled P_0, which was used in the tunnel free-stream calculations. It was located near the propeller plane and therefore was affected by the changing propeller slipstream as the propeller thrust was changed. Wall static pressures were used to verify a theoretical velocity correction and to evaluate the already measured velocity change due to the proximity of the P_0 static pressure and the propeller plane.

The windmill condition of the propeller was used as a baseline condition for all differential pressure measurements. Any differential pressure measured at windmill was assumed to be a bias in the measurement due to the installation and was subtracted from the measurements with the propeller thrusting (powered). The wall static-pressure change from windmill and one-dimensional flow equations for the flow outside the propeller slipstream was used to calculate the ratio of local velocity V_{wi} to a reference velocity V_{ref} far upstream of the propeller. This local velocity ratio V_{wi}/V_{ref} was plotted as a function of the axial distance from the propeller plane for the free-stream Mach numbers and thrust levels tested (fig. 47). The change in velocity is significant (as much as a 6-percent change at the propeller plane) and is affected by both thrust and position in the tunnel.

A simplified theoretical formula reported by Glauert (ref. 8) and Pope (ref. 9) relates the effective velocity encountered by the propeller in a solid-wall tunnel (as a ratio to the velocity in the tunnel far upstream of the propeller) to the thrust of the propeller and the size of the propeller in the tunnel:

$$\frac{V'}{V_\infty} = 1 - \frac{\tau \alpha}{2\sqrt{1 + 2\tau}} \tag{B1}$$

where
A   propeller disk area
C   tunnel cross-sectional area
T   propeller thrust
T_c thrust coefficient based on diameter squared instead of propeller disk area, $T/D^2 \rho V_\infty^2$
V'   effective velocity encountered by propeller
V_∞ tunnel velocity far upstream
α A/C
ρ tunnel density
τ thrust coefficient based on propeller disk area $\tau = T/A\rho V_\infty^2 = T_c \times (4/\pi)$

A compressibility correction to the thrust coefficient was shown to be required by Young (ref. 10).

The required thrust coefficient and the velocity equation then become

$$\tau_c = \frac{\tau}{1 - M_\infty^2}$$

and
$$\frac{V'}{V} = 1 - \frac{\tau_c \alpha}{2\sqrt{1 + 2\tau_c}}$$

(B2)

The ratio of measured local propeller-plane velocity (XW/HT = 0 in fig. 47) to reference velocity V_{pp}/V_{ref} is shown as a function of the compressible-thrust coefficient τ_c in figure 48. The theoretical values of V'/V are also shown. Comparison indicates good agreement between the propeller-plane measurement and the theory.

The location (XW/HT = -0.117) of the static tap P_0 (fig. 46) used in the free-stream velocity calculation is near the propeller plane, not far upstream as assumed in the theoretical formula for calculating the effective velocity of the propeller. The variation of velocity change (which was cal-culated from the local pressure changes) with axial position was used to determine how much of the theoretical velocity change due to thrust had been already measured by the P_0 pressure tap. The velocity change at the same axial location as the P_0 measurement was interpolated from the wall measurements. The ratio of this wall free-stream velocity change to each measured wall velocity change $\Delta V_0 / \Delta V_{wi}$ is plotted as a function of the axial distance from the propeller plane in figure 49. The plot indicates that at the location of the free-stream static-pressure tap, approximately half of the velocity change occurring at the propeller plane (XW/HT = 0) has already taken place. The ratio of the wall free-stream velocity change to the propeller-plane velocity change $\Delta V_0 / \Delta V_{pp}$ is plotted as a function of the compressible-thrust coefficient τ_c in figure 50. The plot shows that the scatter seen at the propeller plane (and the other locations) is associated with low thrust levels, where the accuracy of the differential pressure measurements limits the velocity change information.

Therefore the required correction to free-stream V'/V_0 is actually only half of the theoretical V'/V_∞ value. The propeller data presented in this report have this reduced correction applied to the efficiency and advance ratio.

13

APPENDIX C – ADJUSTED METHOD USED TO OBTAIN MEASURED PROPELLER THRUST

The propeller at windmill (no power) was used as a reference condition to correct the thrust readings from the rotating balance. This procedure was required to overcome a slow thermal drift in the rotating-balance thrust reading. Windmill reference conditions were established during special tunnel runs by using the strut-mounted force system. Dimensionless propeller-thrust coefficient and advance ratio were used to eliminate possible small variations in windmill operation due to any day-to-day changes in wind tunnel conditions. After the reference windmill conditions were established (figs. 51 and 52), incremental thrust data were obtained by using the rotating balance in a windmill-power-windmill test sequence. At each desired power point, the PTR was first windmilled; then a power point was taken and then a second windmill point. The average thrust from the two windmill points was subtracted from the thrust at the power point to obtain an incremental propeller thrust. Since the drift in thrust output from the rotating balance was very small over the short time period required to obtain the three data points, any significant error in the incremental thrust could be eliminated. The incremental thrust from the rotating balance was combined with the reference windmill conditions (determined in the earlier tests with the strut-mounted force system) to establish the final propeller operating conditions. The procedure and equations that were used to establish the final performance conditions were as follows:

(1) Obtain an average reference windmill advance ratio $J_{P,R}$ for each blade angle and Mach number from the powered runs.

(2) Obtain the reference effective-thrust coefficient CT_{efr} at the windmill advance ratio of the powered run by using the effective-thrust-coefficient-at-windmill curve generated in the windmill drag runs, (fig. 51 for the SR-2 propeller and fig. 52 for the SR-3 propeller).

(3) Calculate and print performance summary tables based on the reference advance ratio J_{PR} and reference effective thrust coefficient $C_{T,efr}$. The thrusts at the power points are adjusted for thermal zero shift according to following the equation:

$$C_{T,P} = C_{T,B} - C_{T,WB}\left(\frac{J_P^2}{J_{P,W}^2}\right) + C_{T,efr}\left(\frac{J_P^2}{J_{P,R}^2}\right)$$

where
$C_{T,B}$ power-point thrust coefficient (rotating balance)
$C_{T,P}$ adjusted thrust coefficient (rotating balance)
$C_{T,WB}$ average of effective thrust coefficients from windmill points before and after power point (rotating balance)
J_P power point advance ratio
$J_{P,W}$ average of advance ratios from windmill points before and after power point
and $J_{P,R}$ and $C_{T,efr}$ are described in items (1) and (2).

To verify that the above procedure produces good results, propeller data were compared. Identical propeller hardware (SR-1 with a conic spinner) was tested at Mach 0.80 in both the NASA Lewis 8- by 6-Foot Supersonic Wind Tunnel and the UTRC 8-ft octagonal tunnel by using different propeller test rigs

14

(PTR). The NASA data were reduced by using the adjusted performance method just described. Figure 53 presents a comparison of data from these two facilities at 90- and 100-percent design power loading. The data agree within about 1 percent at 90-percent loading, and at design the agreement is even better. A slight extrapolation of the UTRC data was required to obtain the design power-loading condition due to the limited power capability of the PTR of that facility. Other comparisons of data at the takeoff Mach number of 0.20 at these two facilities are shown in figures 41 to 44 and are discussed in the main text. These data also agree within 1 percent.

REFERENCES

1. Jeracki, R.J.; Mikkelson, D.C.; and Blaha, B.J.: Wind Tunnel Performance of Four Energy Efficient Propellers Designed for Mach 0.8 Cruise. SAE Paper 790573, Apr. 1979 (NASA TM-79124).

2. Whitlow, Jr., J.B.; and Sievers, G.K.: Fuel Savings Potential of the NASA Advanced Turboprop Program. NASA TM-83736, 1984.

3. Stefko, G.L.; and Jeracki, R.J.: Wind Tunnel Results of Advanced High Speed Propellers in the Takeoff, Climb, and Landing Operating Regimes. AIAA Paper 85-1259, July 1985 (NASA TM-87054).

4. Rohrbach, C., F.B. Metzger, D.M. Black, and R.M. Ladden: Evaluation of Wind Tunnel Performance Testing of an Advanced 45° Swept Eight-Bladed Propeller at Mach Numbers from 0.45 to 0.85. NASA CR-3505, 1982.

5. Mikkelson, D.C., B.J. Blaha, G.A. Mitchell, and J.E. Wikete: Design and Performance of Energy Efficient Propellers for Mach 0.8 Cruise. SAE Paper 770458, Mar. 1977 (NASA TM X-73612).

6. Aiello, R.A.: NASA Lewis 10- by 10-Foot Supersonic Wind Tunnel. NASA TM X-71625, 1974.

7. Black, D.; Menthe, R.W.; and Wainauski, H.S.: Design and Performance Testing of an Advanced 30° Swept, Eight Bladed Propeller at Mach Numbers from 0.2 to 0.85. NASA CR-3047, 1978.

8. Glauert, H.: Wind Tunnel Interference on Wings, Bodies, and Airscrews. R.&M. No. 1566, British A.R.C., 1933.

9. Pope, A.: Wind-Tunnel Testing. John Wiley and Sons, New York, 1954.

10. Young, A.D.: Note on the Application of the Linear Perturbation Theory to Determine the Effect of Compressibility on the Wind Tunnel Constraint on a Propeller. R.&M. No. 2113, British A.R.C., 1944.

TABLE I. – DESIGN CHARACTERISTICS AND PLANFORMS OF SR-2 AND SR-3 MODEL PROPELLERS
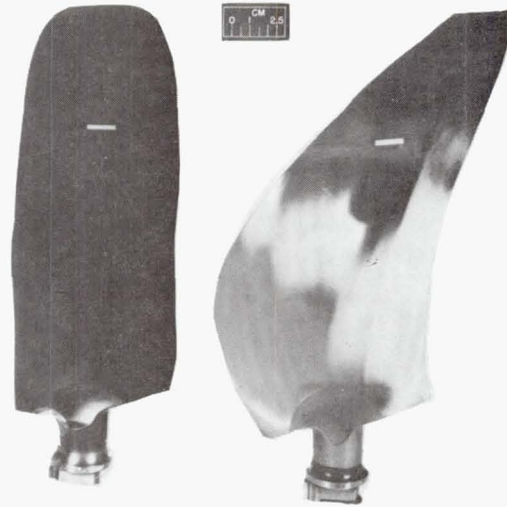
	SR-2	SR-3
Number of blades	8	8
Tip sweep angle, deg	0	45
Reference diameter, cm (in.)	62.2 (24.5)	62.2 (24.5)
Tip speed, m/sec (ft/sec)	244 (800)	244 (800)
Power loading, kW/m^2 (shp/ft^2)	301 (37.5)	301 (37.5)
Activity factor	203	235
Integrated design lift coefficient	0.081	0.214
Airfoils	NACA 16 and 65/CA	NACA 16 and 65/CA
Ratio of nacelle maximum diameter to propeller diameter	0.35	0.35
Cruise design Mach number	0.80	0.80
Cruise design advance ratio	3.06	3.06
Cruise design power coefficient	1.7	1.7
Measured cruise design net efficiency, percent	76	78
Measured cruise noise level, dB	151	146

TABLE II. – DIMENSIONS OF TEST SPINNERS, NACELLE, AND WINDSCREEN

$[R_N = 11.05 \text{ cm } (4.35 \text{ in.}).]$
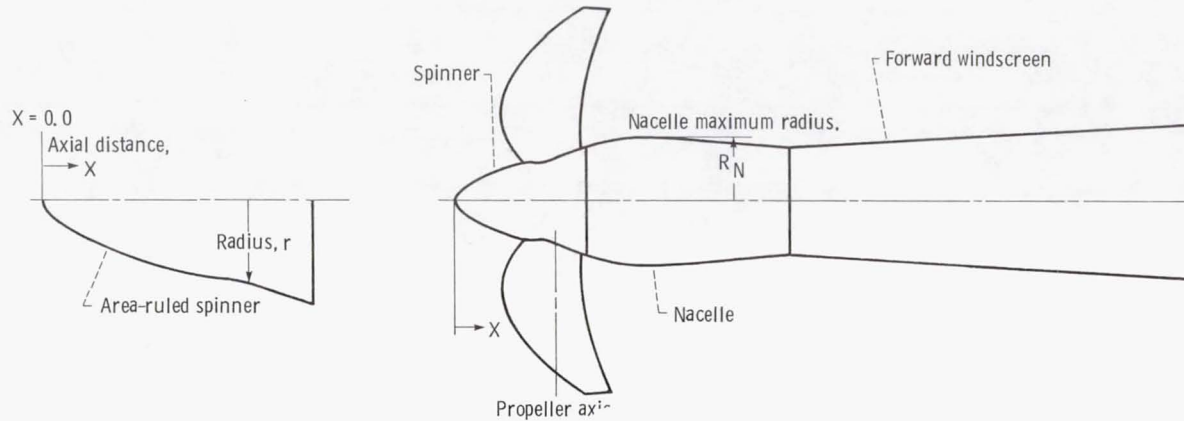
Area-ruled spinners					Nacelle					Forward windscreen	
SR-2		SR-3			Forward		Aft				
Straight blade		45°-swept blade			X/R_N	r/R_N	X/R_N	r/R_N		x/R_N	r/R_N
X/R_N	r/R_N	X/R_N	r/R_N		2.199	0.860	3.366	0.999		5.417	0.865
0.000	0.000	0.000	0.000		2.216	.866	3.596	.990		8.659	1.046
.081	.120	.081	.119		2.239	.873	3.825	.975			
.138	.168	.138	.168		2.262	.881	4.055	.956			
.253	.246	.253	.246		2.285	.888	4.285	.933			
.368	.310	.368	.310		2.308	.895	4.515	.911			
.598	.414	.598	.414		2.331	.902	4.745	.894			
.828	.497	.828	.497		2.354	.908	4.975	.883			
1.057	.568	1.057	.568		2.377	.915	5.205	.874			
1.287	.620	1.092	.577		2.400	.920	5.251	.873			
1.402	.632	1.149	.591		2.423	.926	5.297	.871			
1.517	.639	1.207	.598		2.446	.931	5.400	.871			
1.667	.673	1.264	.597		2.561	.946	------	------			
1.747	.701	1.322	.595		2.676	.970	------	------			
1.977	.784	1.379	.597		2.791	.982	------	------			
2.184	.857	1.437	.606		2.906	.990	------	------			
------	------	1.494	.619		3.136	.999	------	------			
------	------	1.552	.636		3.214	1.000	------	------			
------	------	1.609	.654								
------	------	1.667	.673								
------	------	2.184	.857								

TABLE III. – PTR NACELLE AND SPINNER FACE STATIC-PRESSURE LOCATIONS

$[R_N = 11.05$ cm $(4.35$ in.$).]$
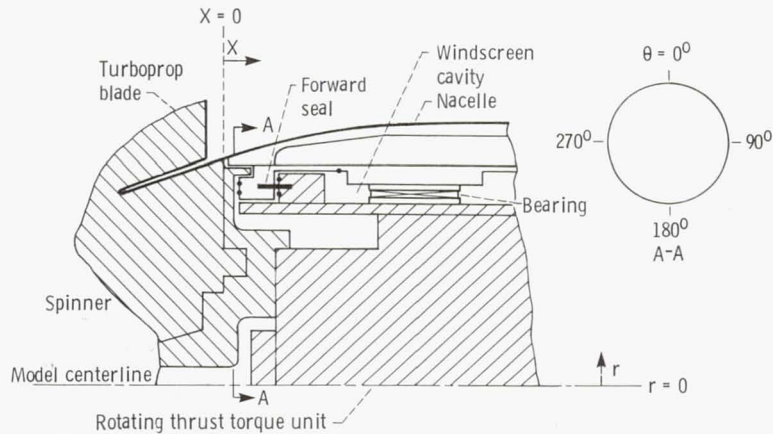
(a) Spinner Face

R/R_N	Angular location, θ, deg
0.6835	0.180
[a].7353	↓
.7861	
.8673	0,900,180,270

[a]Below forward seal.

(b) Nacelle

X/R_N	r/R_N
0.0241	0.8684
.0749	.8848
.1299	.9010
.1880	.9170
.2547	.9326
.3345	.9480
.4276	.9631
.5520	.9780
.7598	.9927
1.0149	1.0000
1.2876	.9949
1.4793	.9848
1.6299	.9745
1.7644	.9642
1.8823	.9537
1.9924	.9431
2.0954	.9323
2.2057	.9215
2.3264	.9105
2.4667	.8994
2.6586	.8882
2.9184	.8768

TABLE IV. - SR-2 PROPELLER TEST-RUN

SCHEDULE

Blade angle at 75-percent radius, deg	Mach number			
	0.10	0.20	0.27	0.34
24.9	X	X	–	–
29.6	X	X	–	–
34.4	X	X	X	–
38.0	X	X	X	–
41.7	X	X	X	X
45.8	–	X	X	X
49.8	–	X	X	X
53.8	–	–	X	X
59.7	–	–	X	X

TABLE V. - SR-3 PROPELLER TEST-RUN SCHEDULE

Blade angle at 75-percent radius, deg	Mach number				
	0.00	0.10	0.20	0.37	0.34
-6.8	X	X	X	–	–
24.6	–	X	X	–	–
29.4	–	X	X	–	–
33.9	–	X	X	X	–
37.3	–	X	X	X	–
41.9	–	X	X	X	–
45.9	–	X	X	X	X
48.3	–	–	X	X	X
51.4	–	–	X	X	X
54.1	–	–	X	X	X
58.3	–	–	X	X	X
62.1	–	–	–	X	X
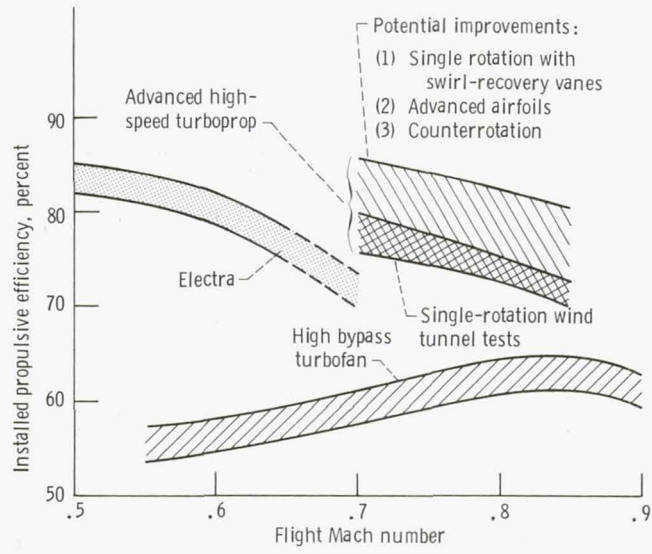
Figure 1. - Installed propulsive efficiency trends of advanced turbo-props compared with equivalent technology turbofans.
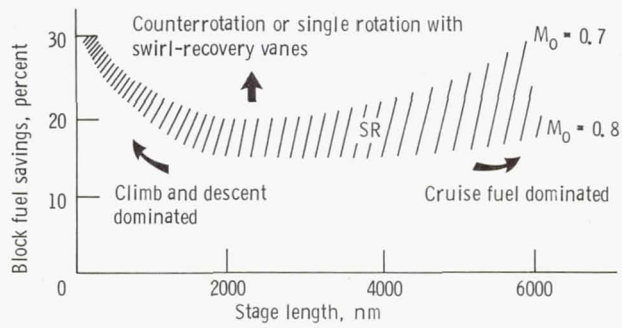
Figure 2. - Fuel savings trends of advanced turboprop aircraft over comparable turbofan aircraft.
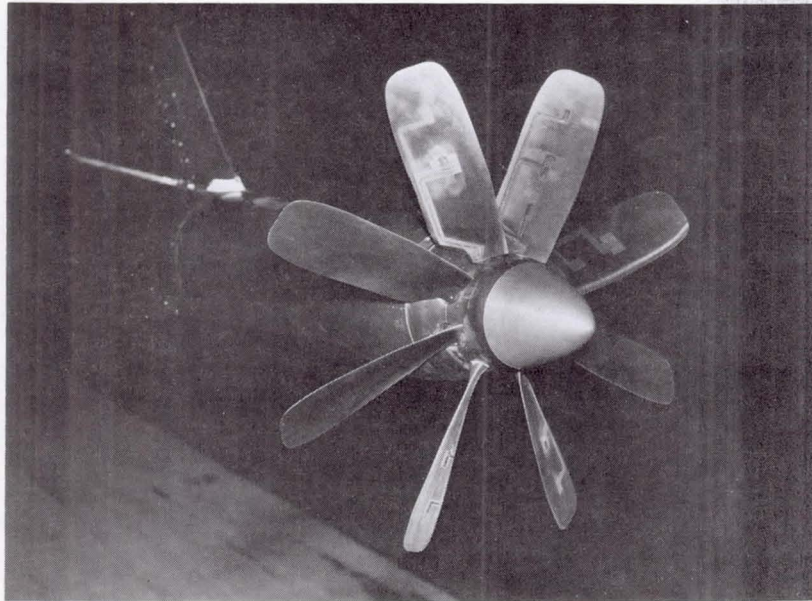
Figure 3. - SR-2 propeller model with straight blades installed in NASA Lewis 10-by 10-Foot Supersonic Wind Tunnel.

Figure 4. - SR-3 propeller model with 45°-swept blades installed in NASA Lewis 10-by 10-Foot Supersonic Wind Tunnel.
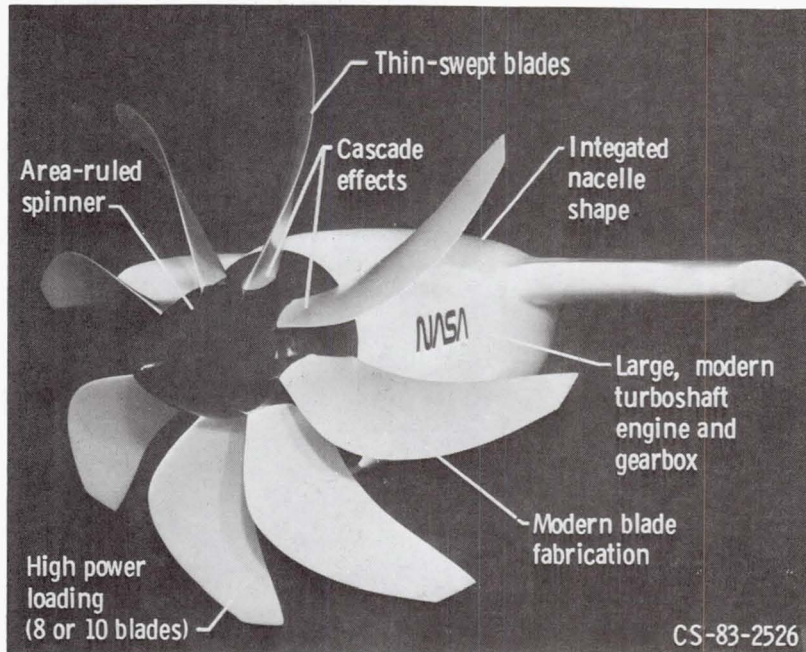
Figure 5. - Aerodynamic design concepts for an advanced high speed turboprop propulsion system.
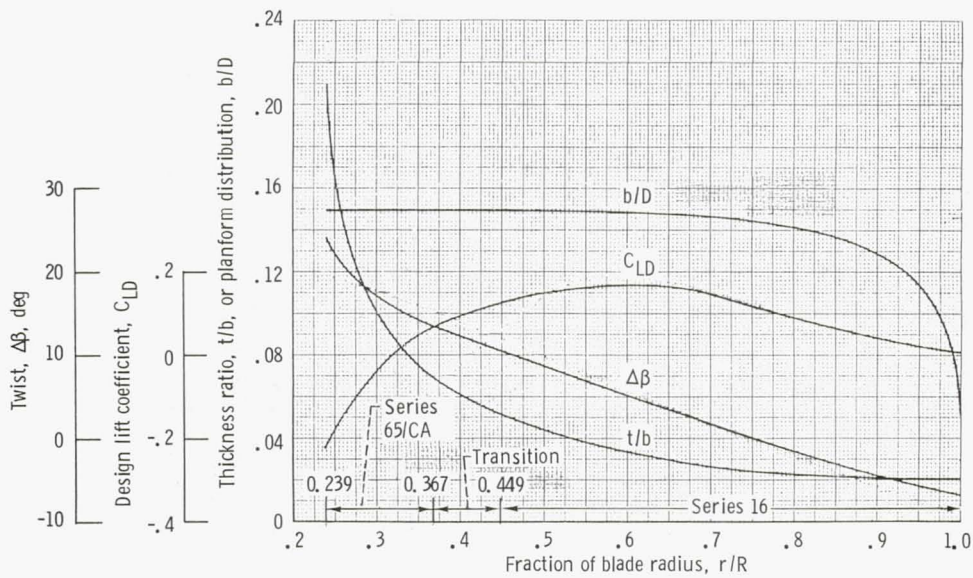
Figure 6. - Variation of propeller design parameters with blade radius for unswept SR-2 propeller. Number of blades, eight; blade activity factor AF = 203; integrated design lift coefficient C_{Li} = 0.08; diameter, 0.62 m (24.5 in.).
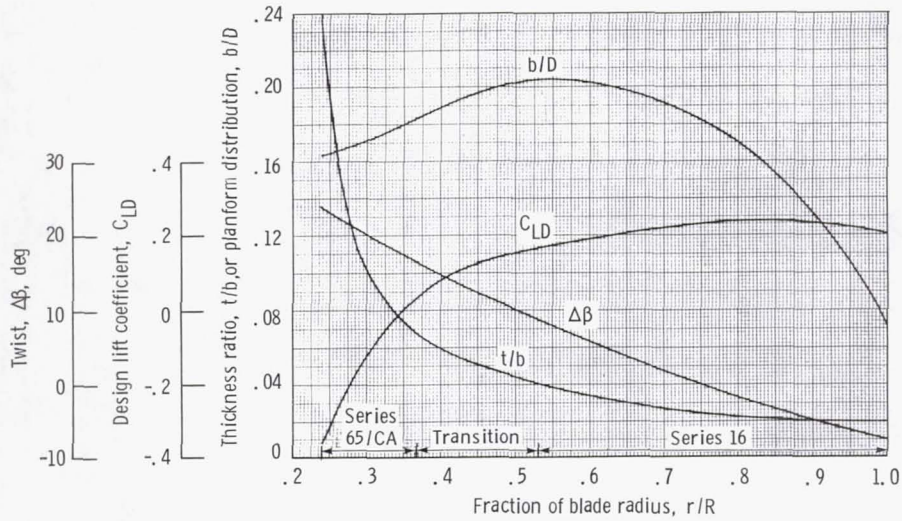
Figure 7. - Variation of propeller design parameters with blade radius for 45^0-swept SR-3 propeller. Number of blades, eight; blade activity factor $AF = 235$; integrated design lift coefficient $C_{Li} = 0.241$; diameter, 0.62 m (24.5 in.).
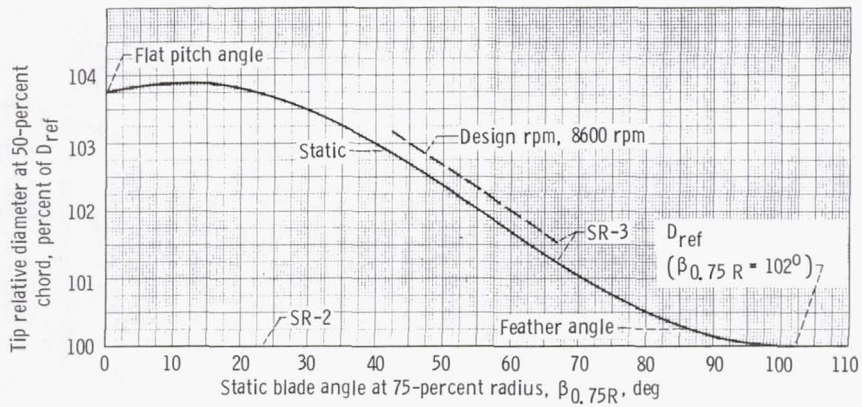
Figure 8. - Variation of relative tip diameter with blade angle and rotation speed. Reference diameter $D_{ref} = 62.23$ cm (24.5 in.).
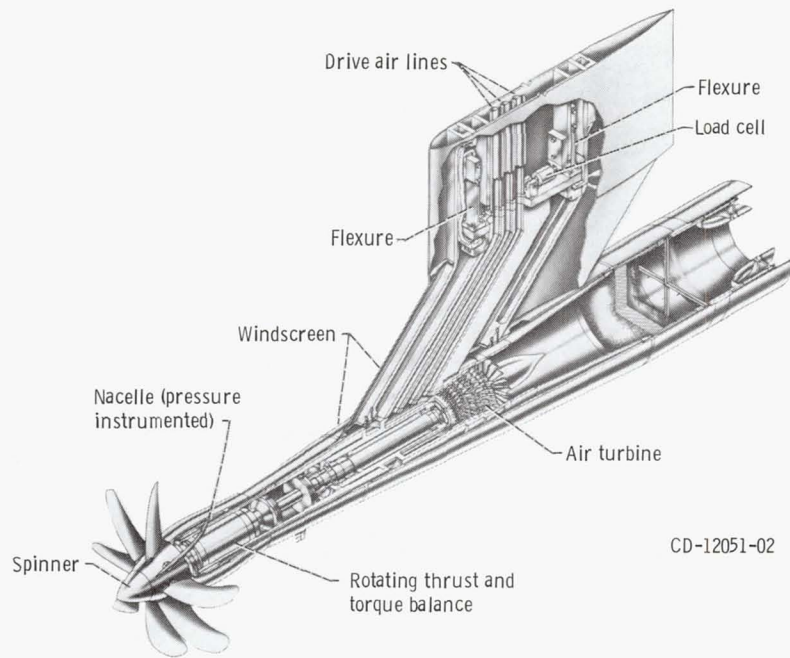
Figure 9. - Cutaway view of Lewis 746-kW (1000-hp) propeller test rig.
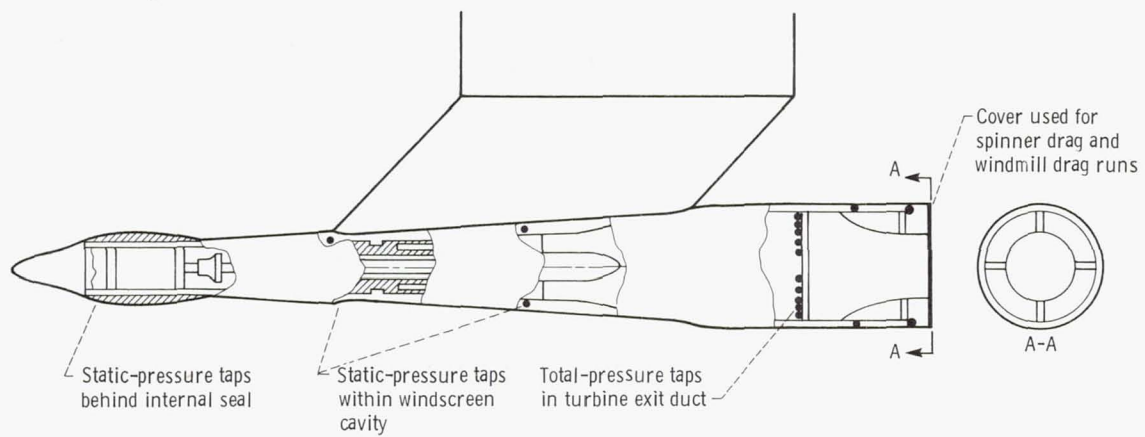
Figure 10. - Internal PTR static-pressure locations.
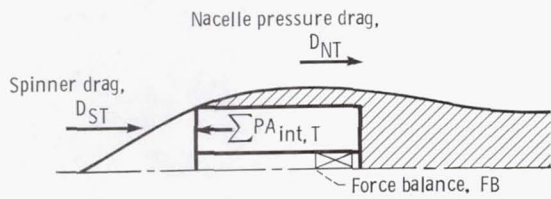
Figure 11. - Forces acting on balance during tare runs. $-D_{ST} = FB_T - \sum PA_{int,T}$; $D_{NT} = \int (p_N - p_0)\, dA$.
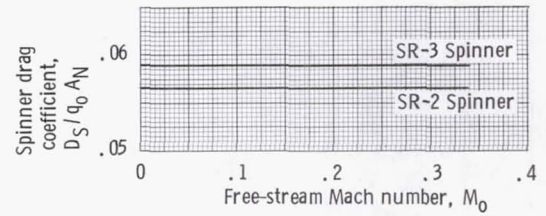
Figure 12. - SR-2 and SR-3 spinner drag coefficient (dummy hub without propeller blades).
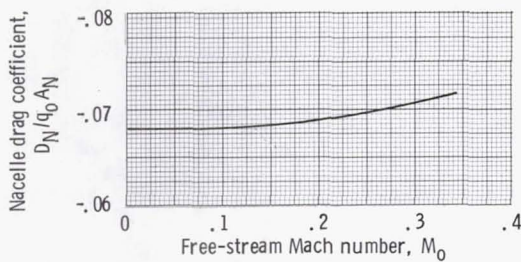
Figure 13. - SR-2 and SR-3 nacelle drag coefficient (dummy hub without propeller blades).
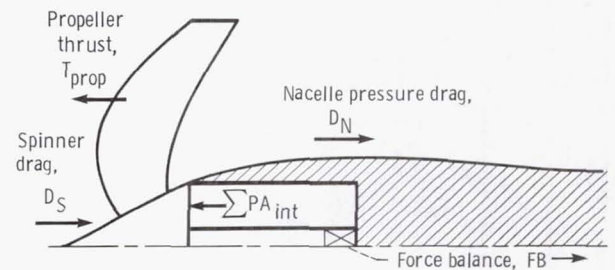
Figure 14. - Forces acting on balance during test runs.
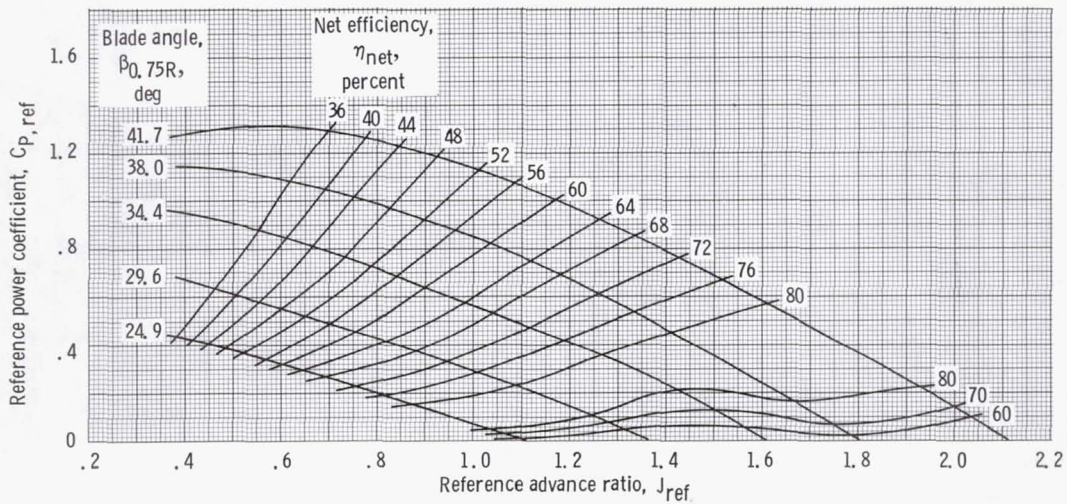
Figure 15. - SR-2 propeller performance map at Mach number of 0.10.
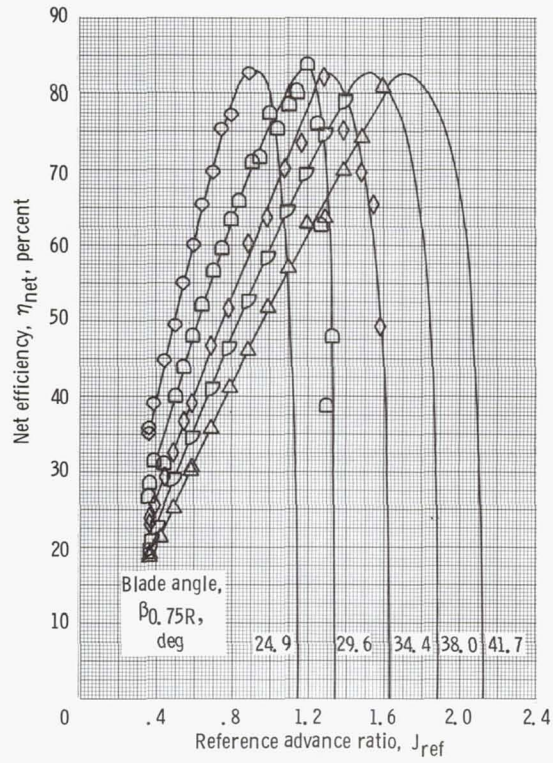
Figure 16. – SR-2 propeller net efficiency as function of
advance ratio at Mach number of 0. 10.
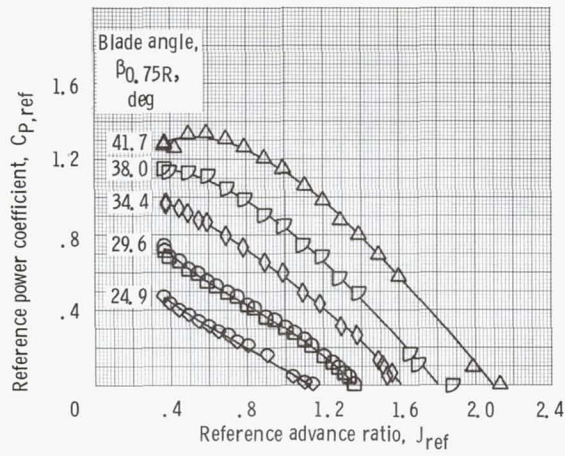
Figure 17. – SR-2 propeller power coefficient as function
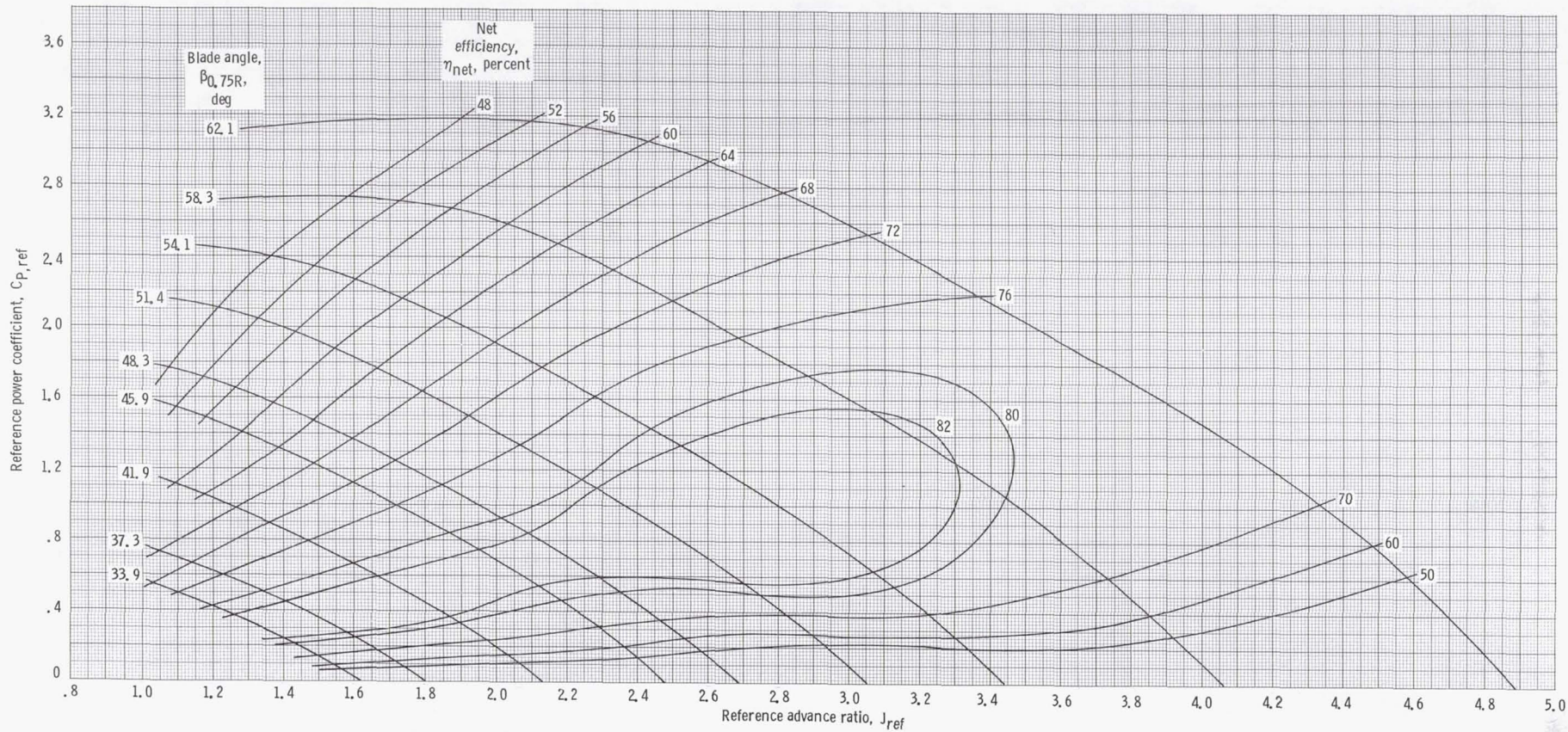of advance ratio at Mach number of 0. 10.
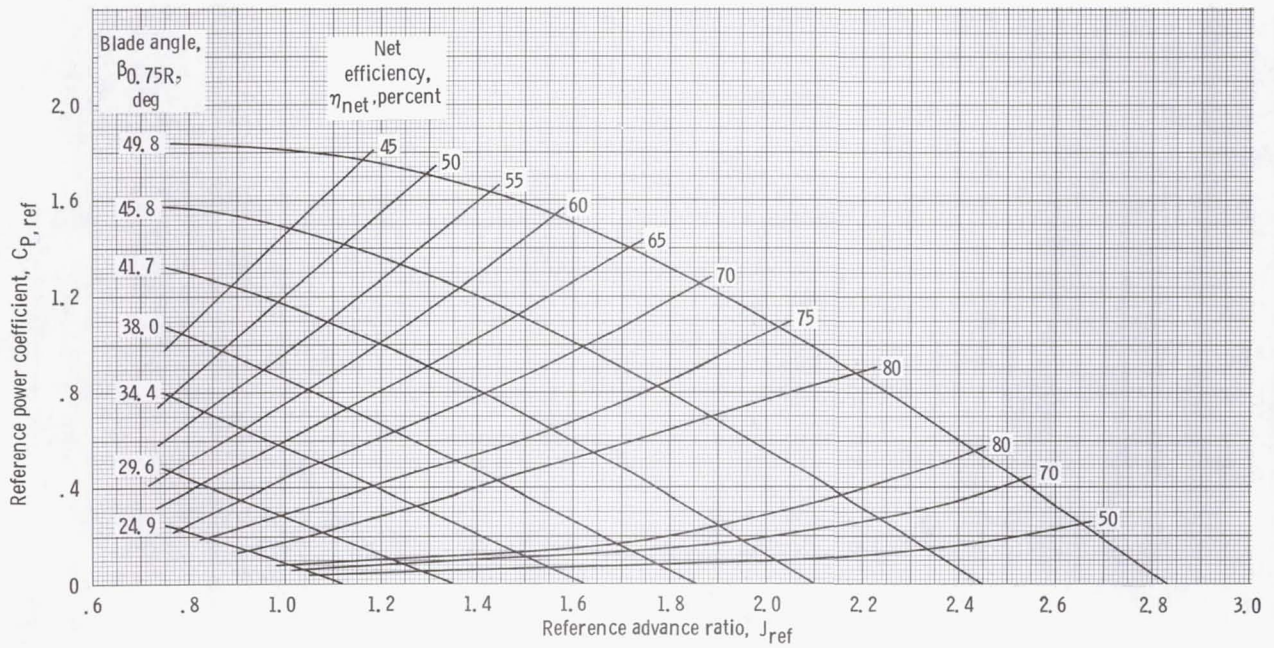
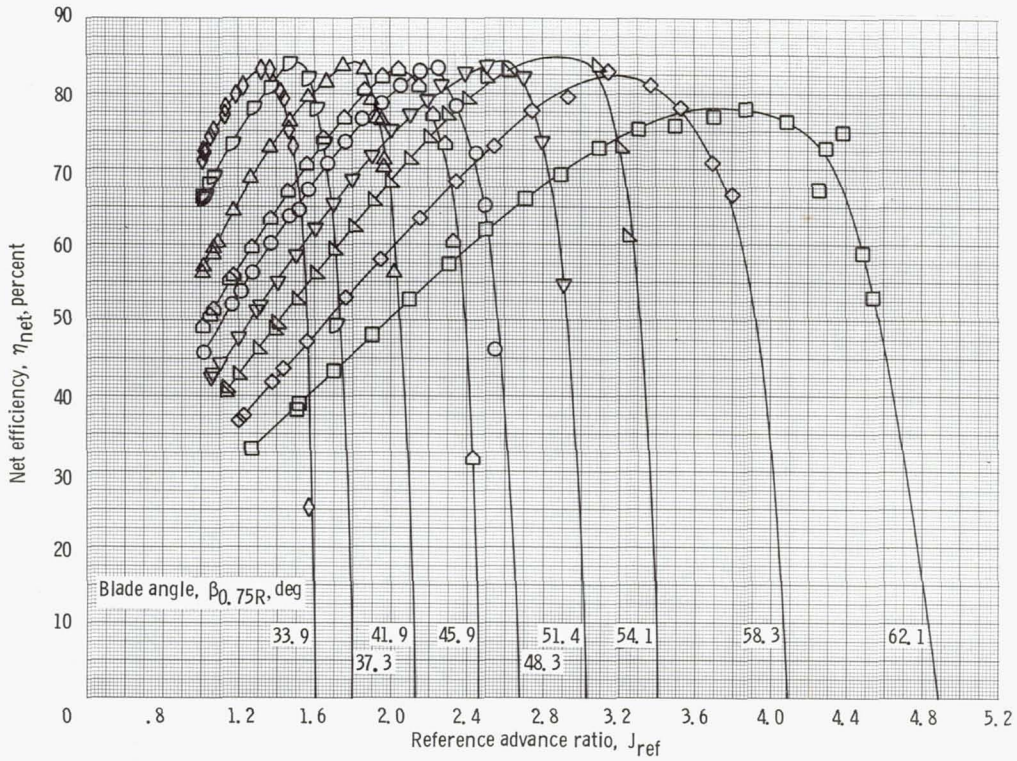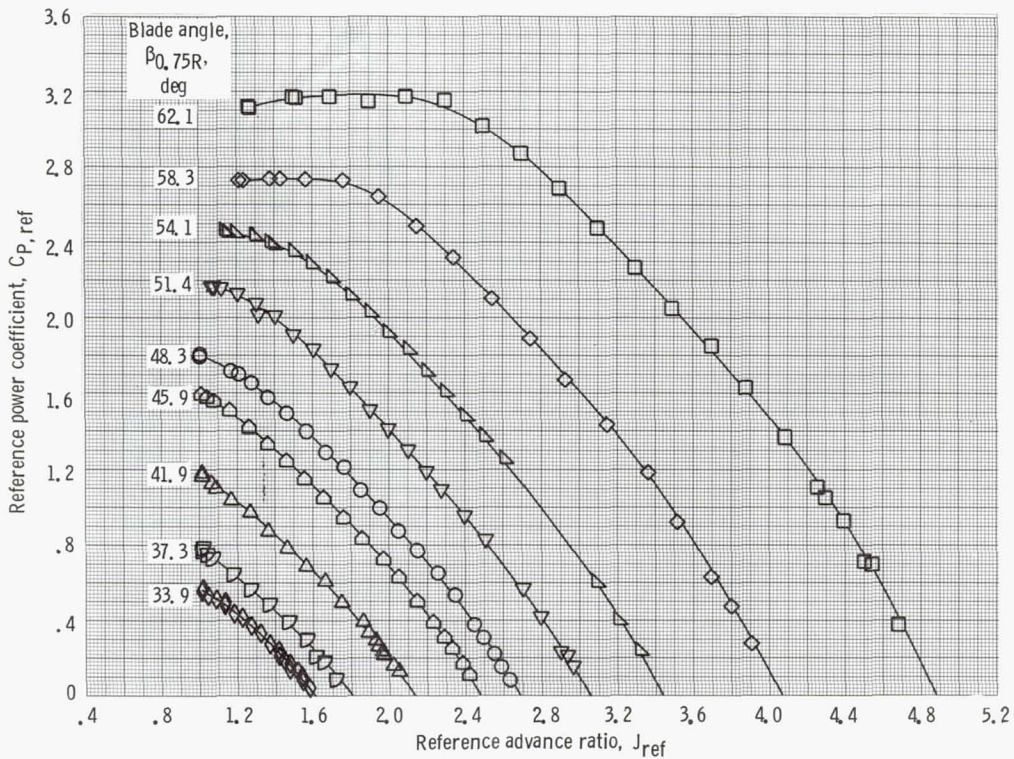Figure 18. – SR-2 propeller performance map at Mach number of 0. 20.
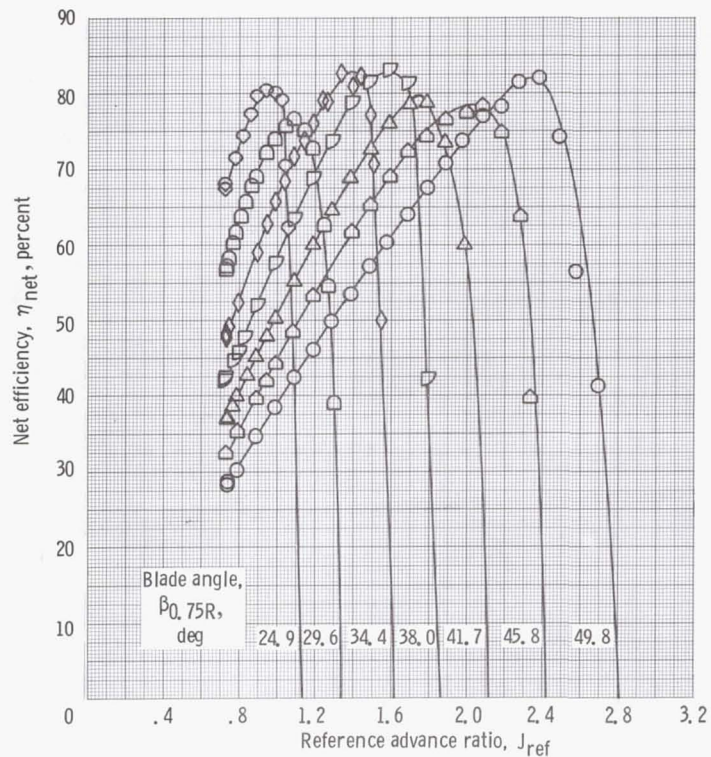
Figure 19. – SR-2 propeller efficiency as function of advance ratio at Mach number of 0. 20.
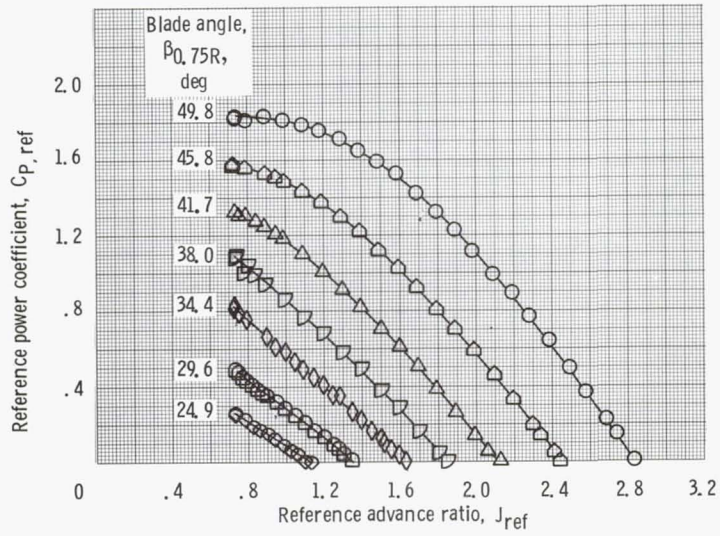
Figure 20. – SR-2 propeller power coefficient as function of advance
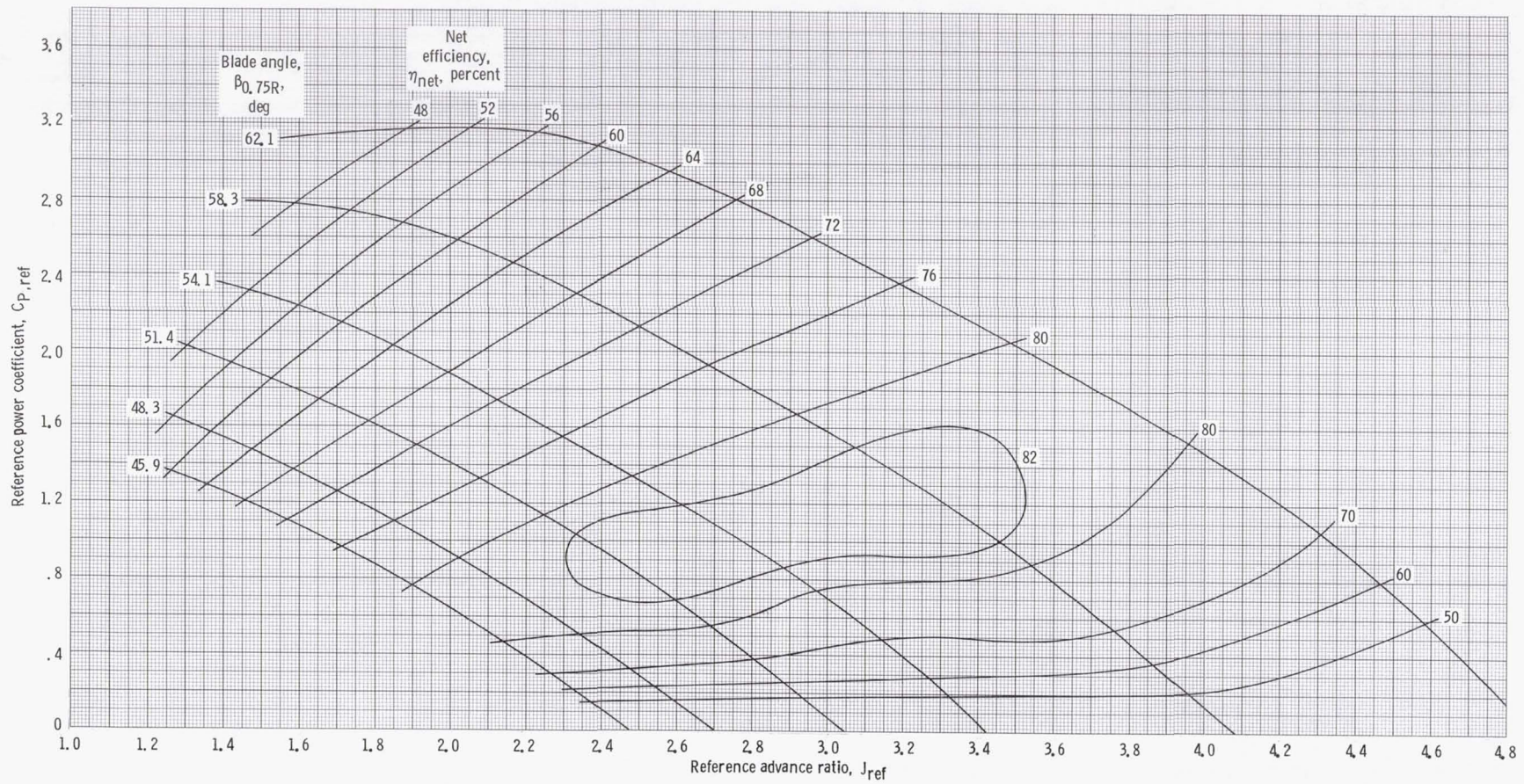ratio at Mach number of 0. 20.
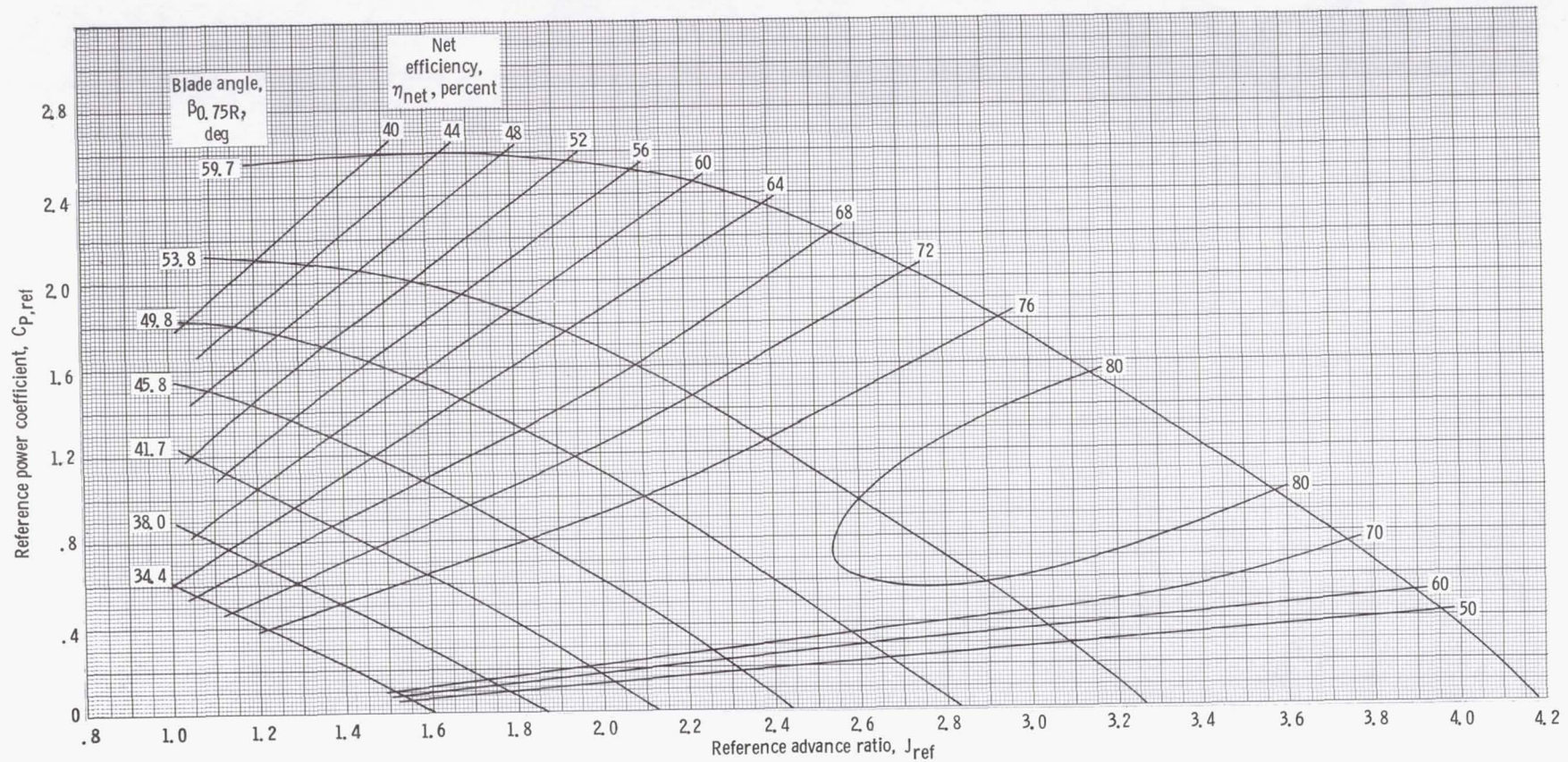
Figure 21. - SR-2 propeller performance map at Mach number of 0.27.
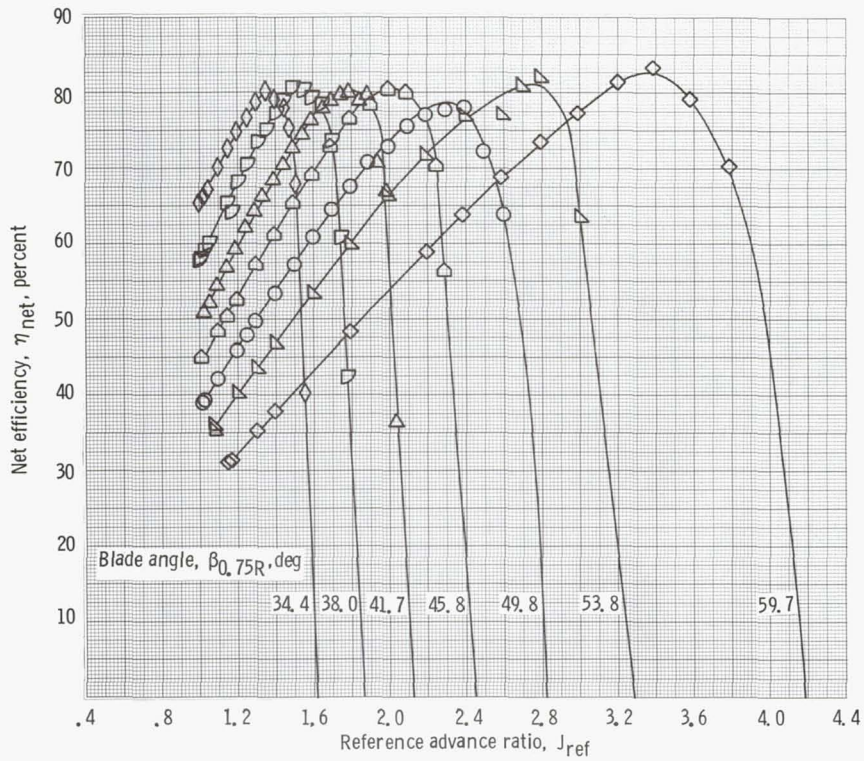
Figure 22. - SR-2 propeller net efficiency as function of advance ratio at Mach number of 0. 27.
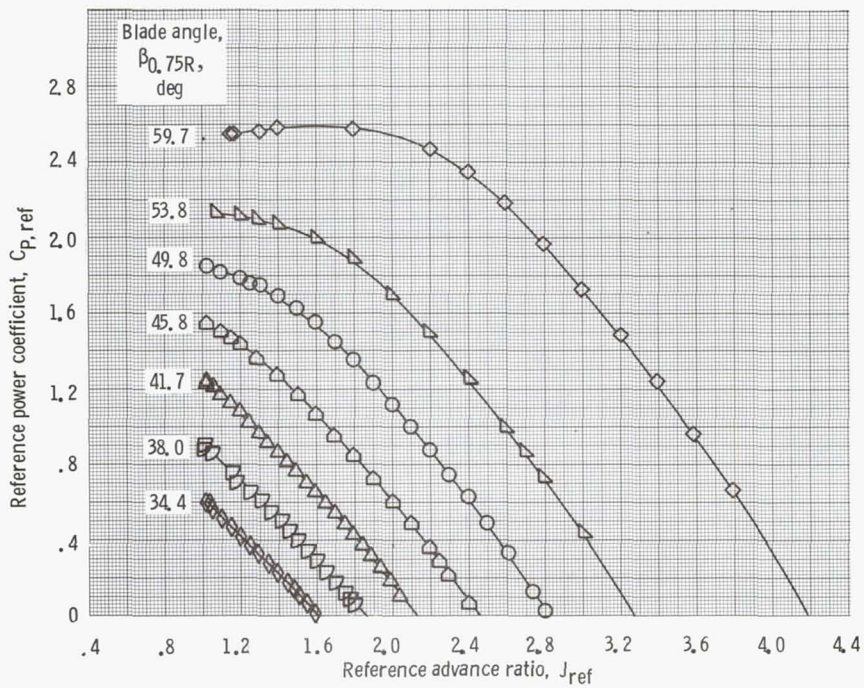
Figure 23. - SR-2 propeller power coefficient as function of advance ratio at Mach number of 0. 27.
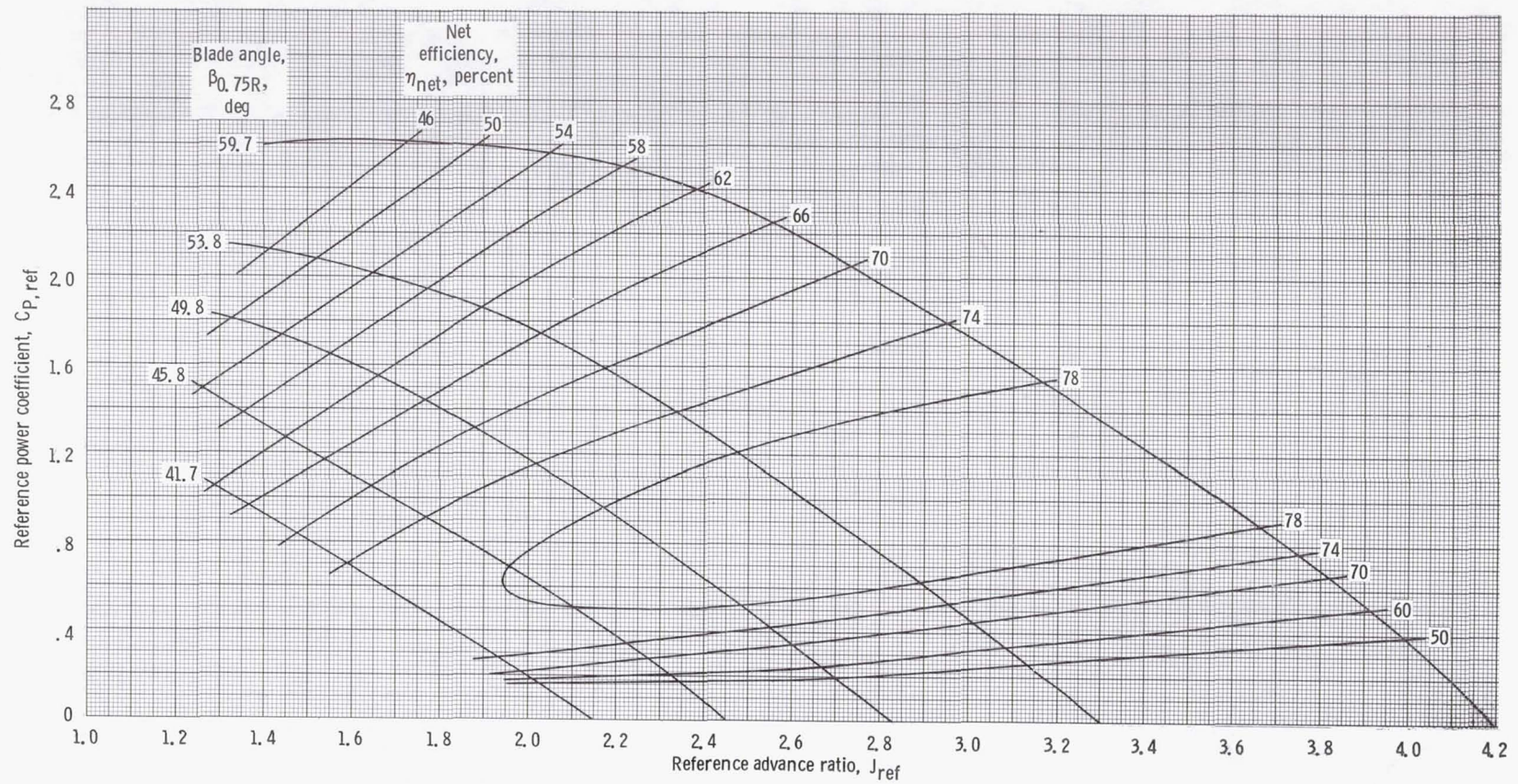
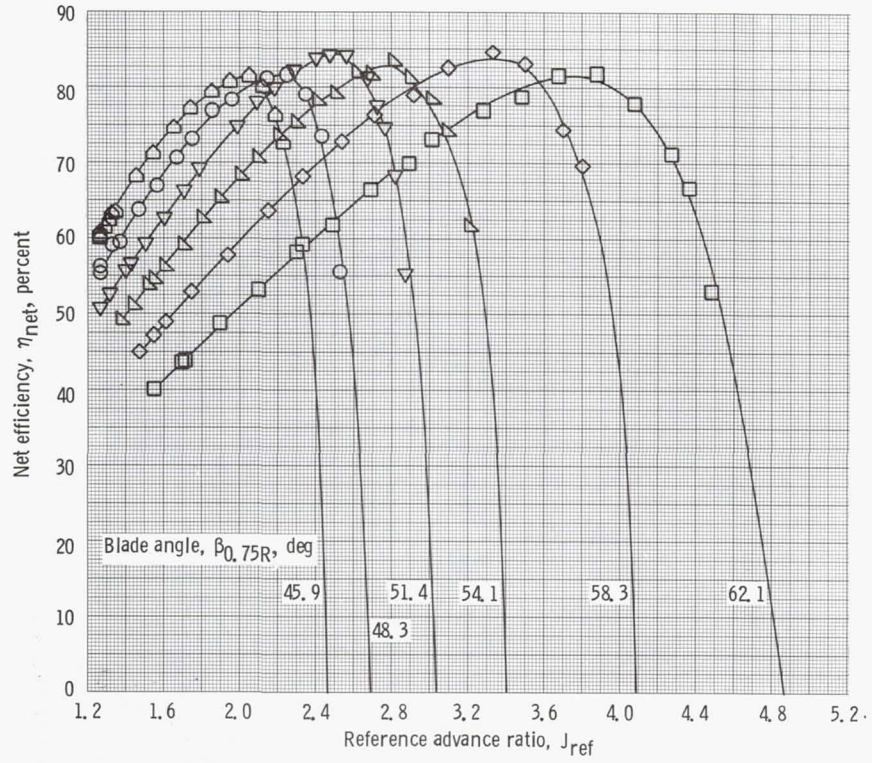Figure 24. – SR-2 propeller performance map at Mach number of 0. 34.
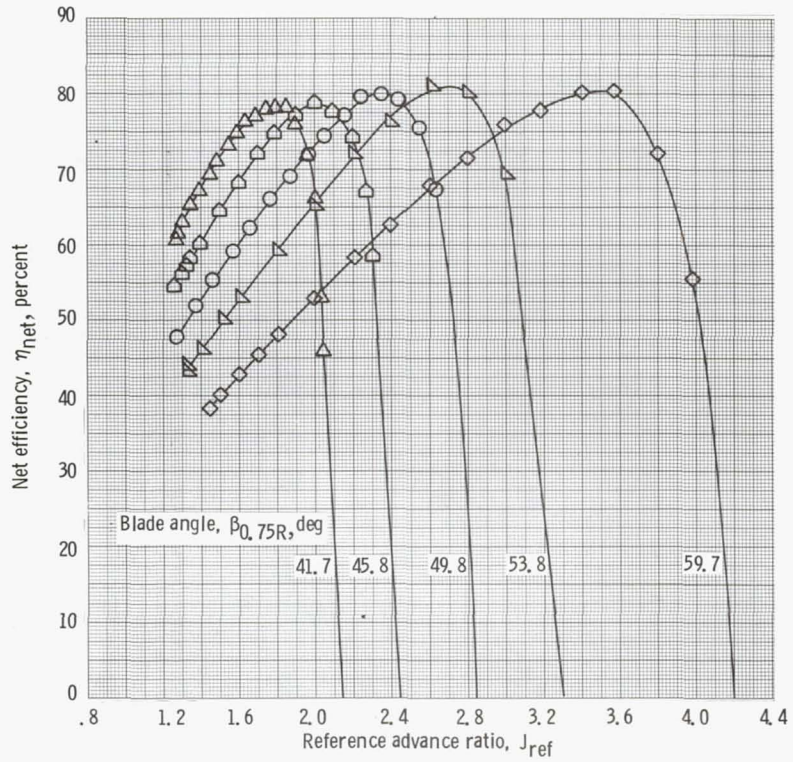
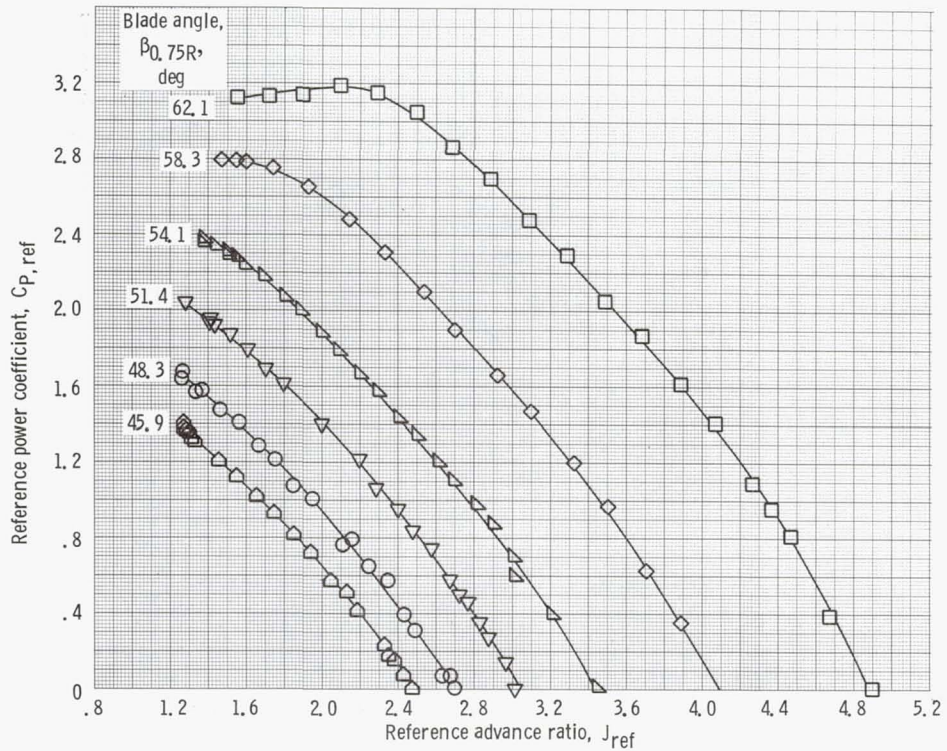Figure 25. - SR-2 propeller net efficiency as function of advance ratio at Mach number of 0. 34.
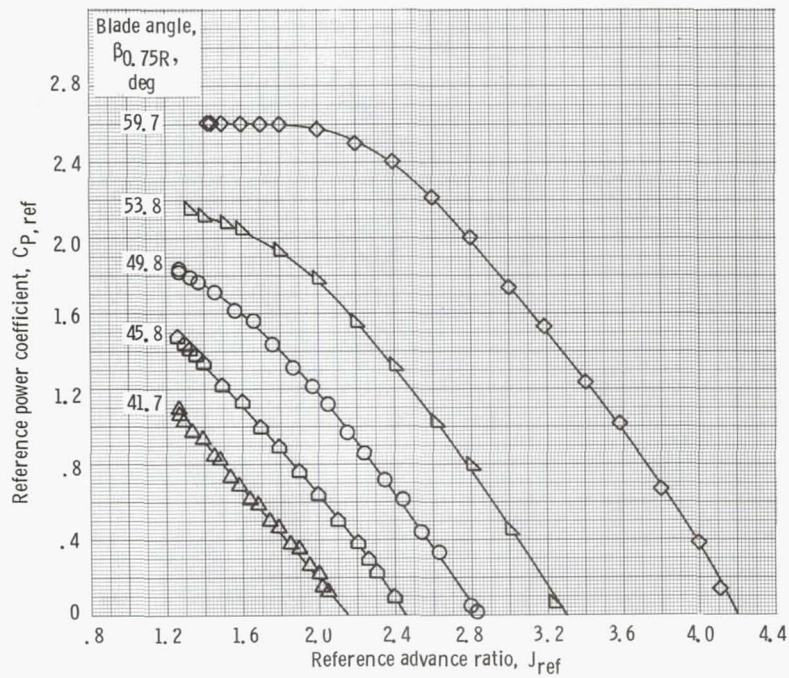
Figure 26. - SR-2 propeller power coefficient as function of advance ratio at Mach number of 0. 34.
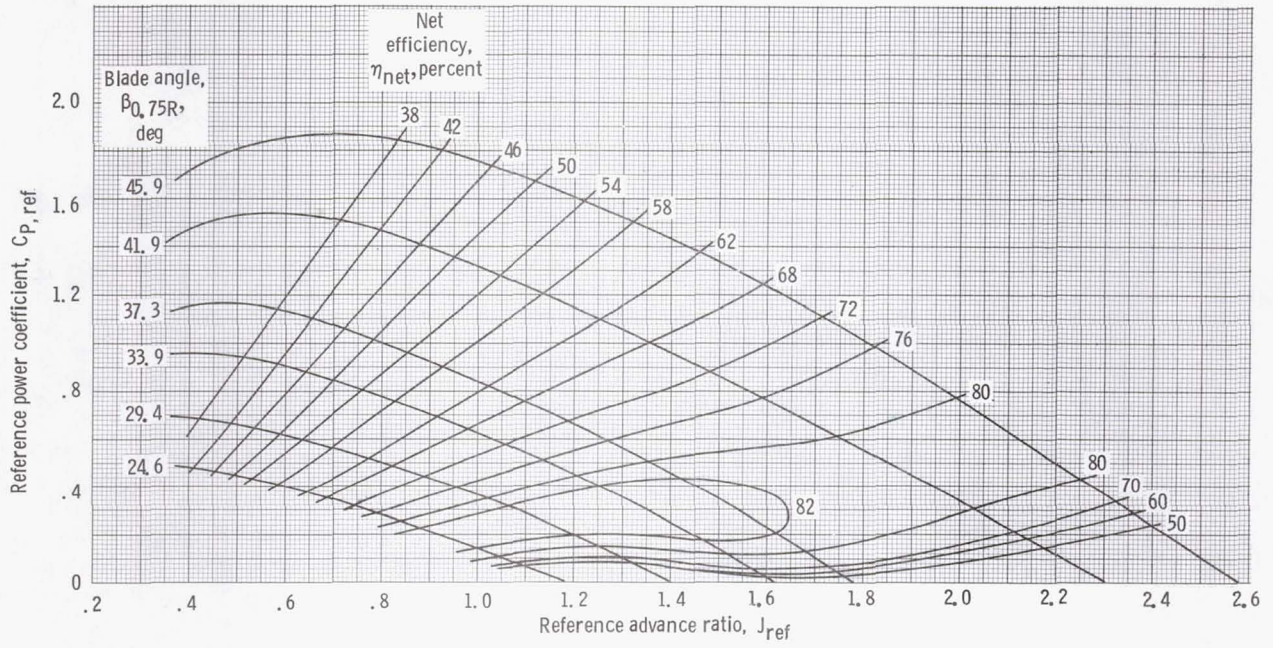
Figure 27. – SR-3 propeller performance map at Mach number Of 0.10.
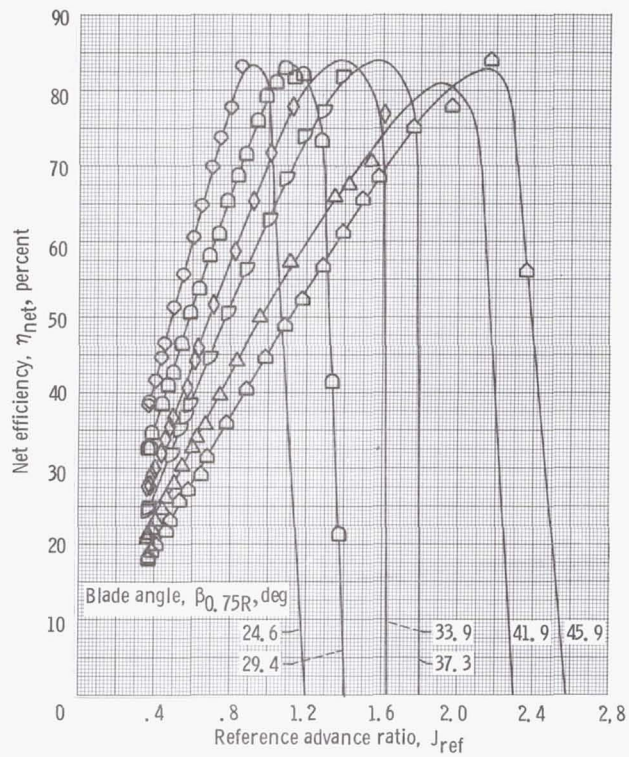
Figure 28. – SR-3 propeller net efficiency as function of advance ratio at Mach number of 0.10.
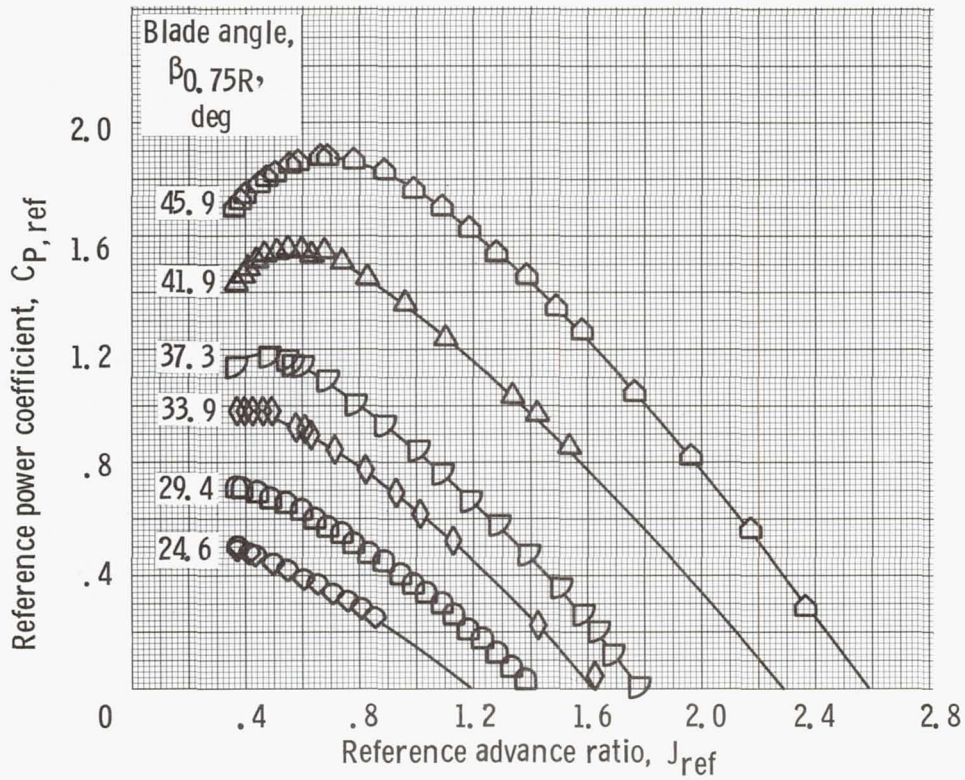
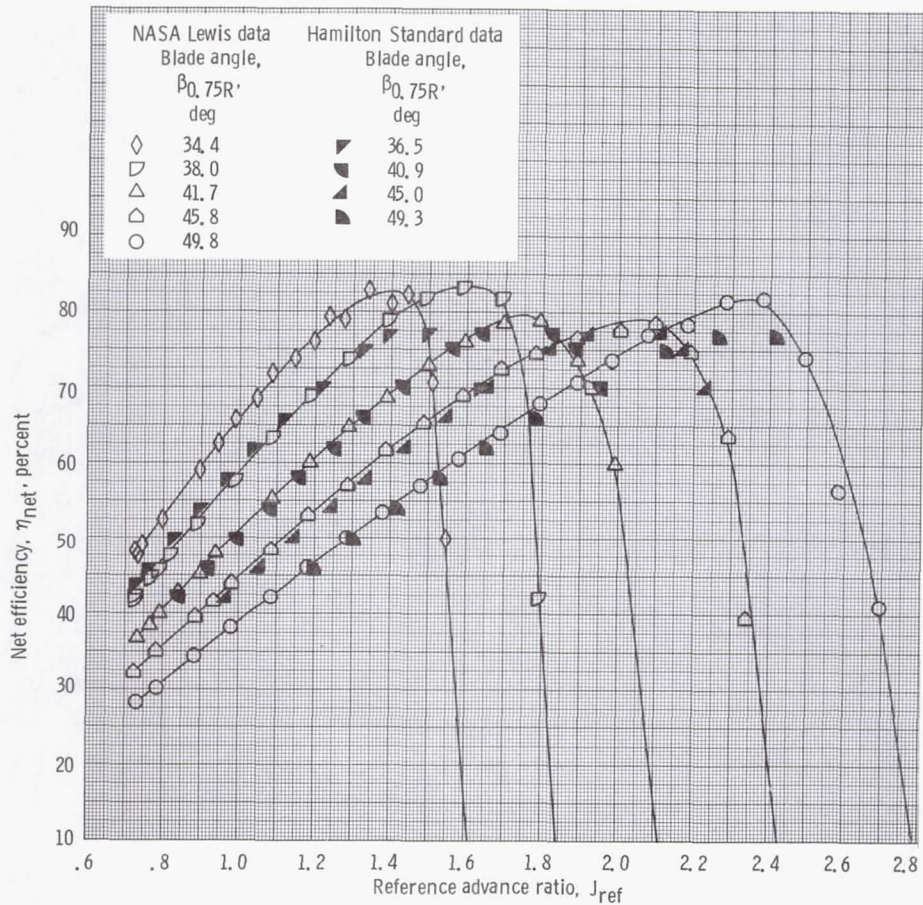Figure 29. – SR–3 propeller power coefficient as function of advance ratio at Mach number of 0.10.
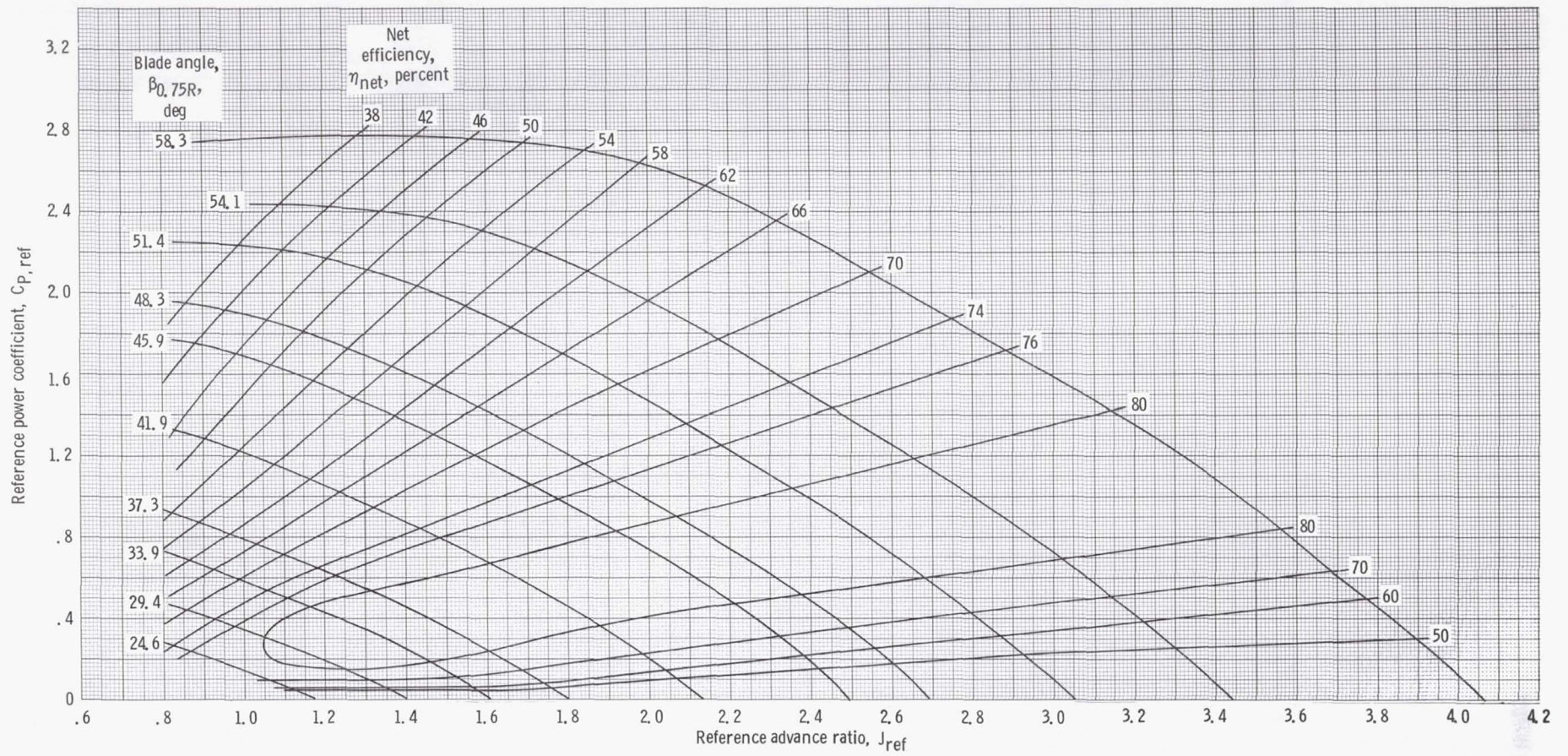
Figure 30. – SR-3 propeller performance map at Mach number of 0.20.
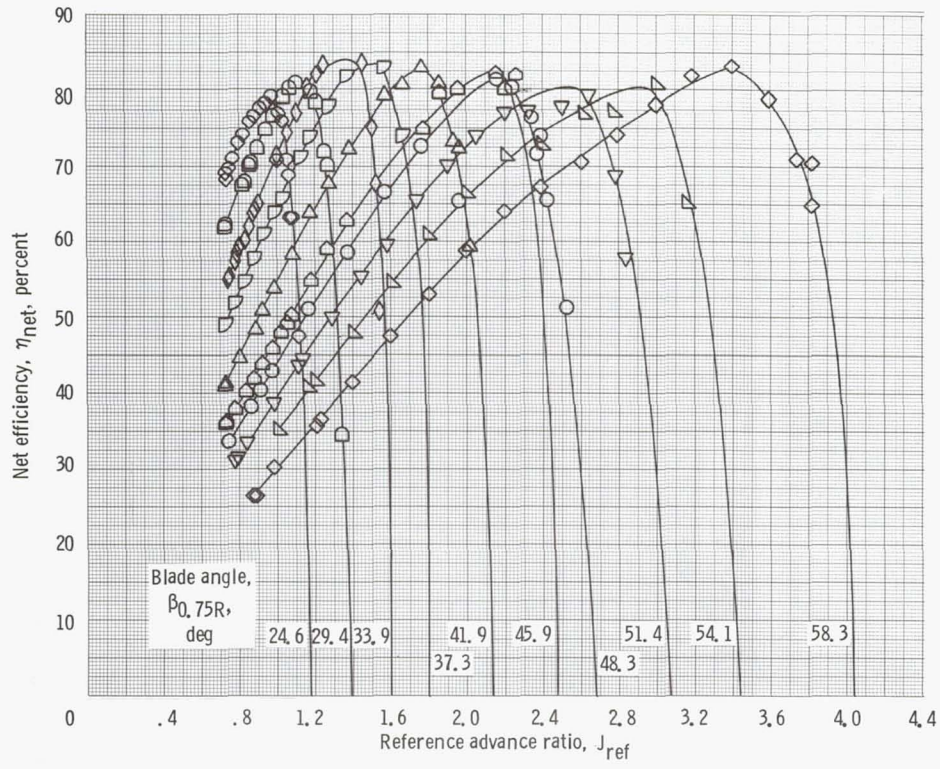
Figure 31. – SR-3 propeller net efficiency as function of advance ratio at Mach number of 0. 20.
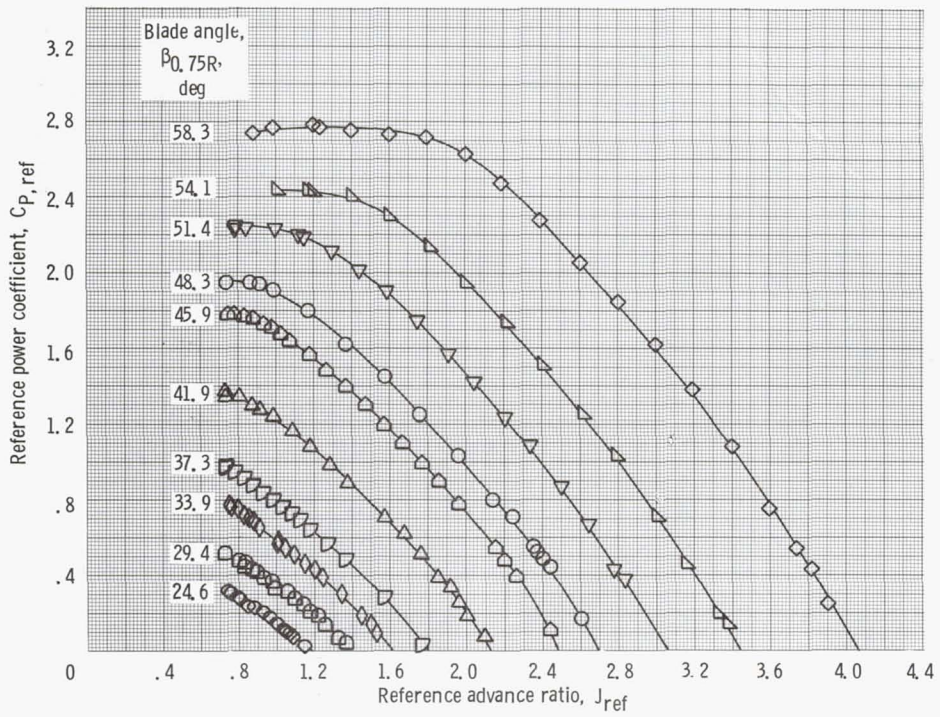
Figure 32. – SR-3 propeller power coefficient as function of advance ratio at Mach number of 0. 20.

Figure 33. - SR-3 propeller performance map at Mach number of 0.27.

Figure 34. – SR-3 propeller net efficiency as function of advance ratio at Mach number of 0. 27.

Figure 35. – SR-3 propeller power coefficient as function of advance ratio at Mach number of 0. 27.

Figure 36. – SR-3 propeller performance map at Mach number of 0. 34.

Figure 37. – SR-3 propeller net efficiency as function of advance ratio at Mach number of 0. 34.

Figure 38. – SR-3 propeller power coefficient as function of advance ratio at Mach number of 0. 34.
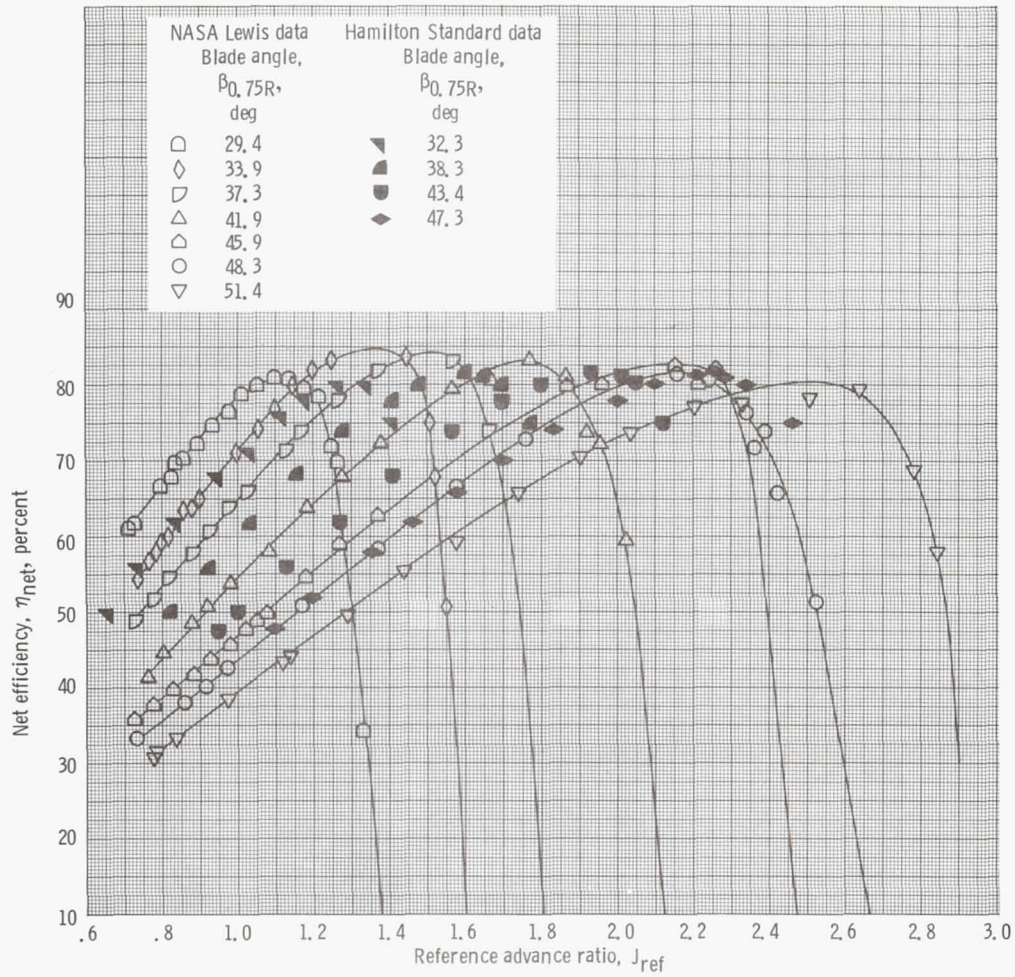
Figure 39. - SR-2 propeller efficiency comparison between two different wind tunnels and propeller test rigs at Mach 0. 20. Hamilton Standard data are from faired curves.
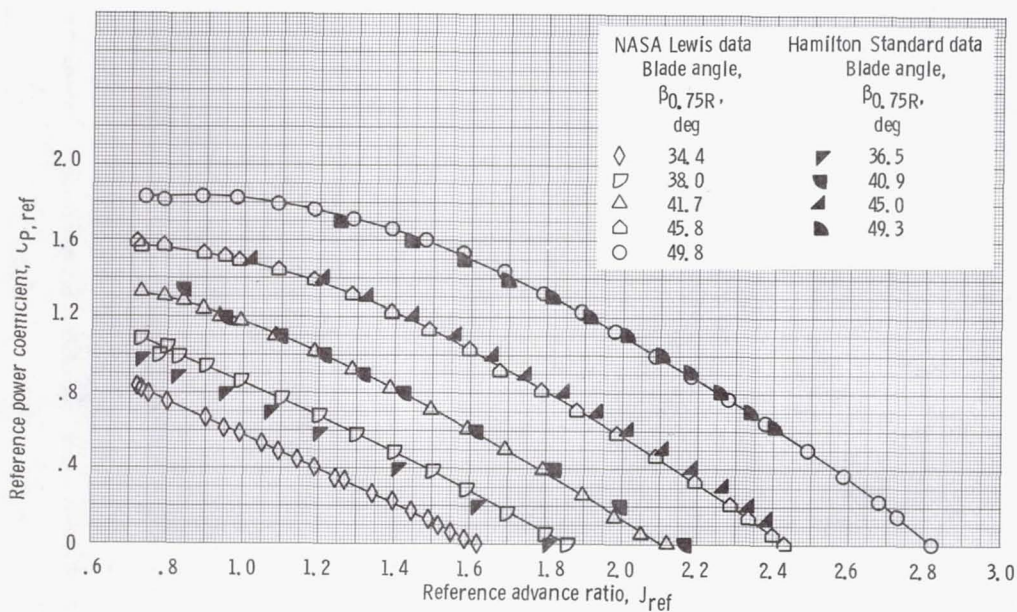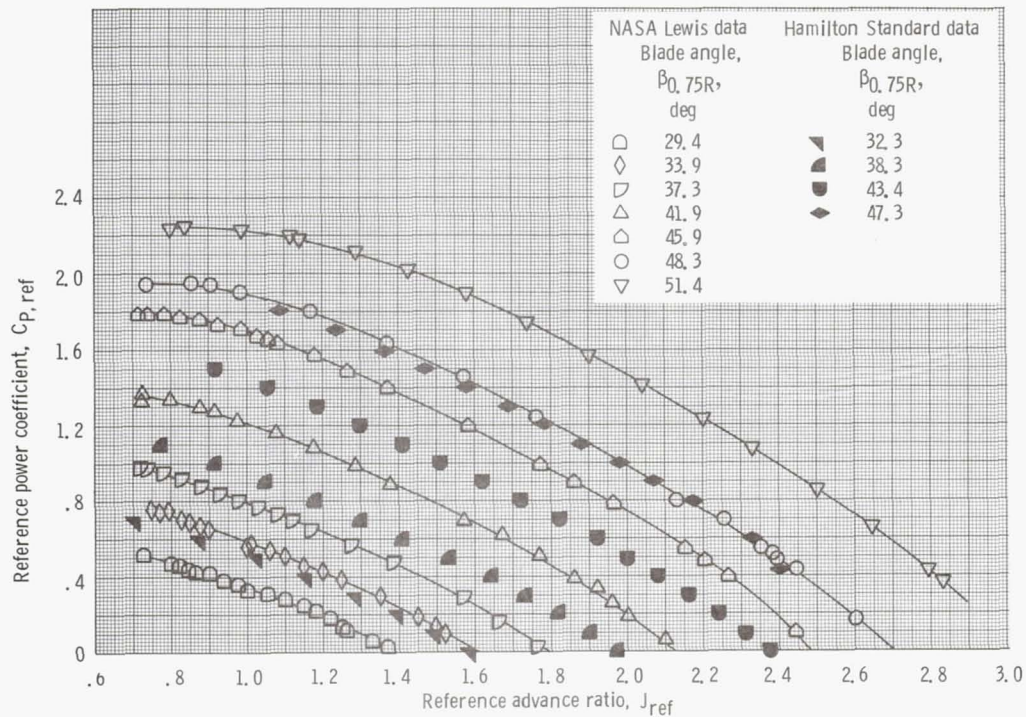

Figure 40. - SR-2 propeller power coefficient comparison between two different wind tunnels and propeller test rigs at Mach 0. 20. Hamilton Standard data are from faired curves.
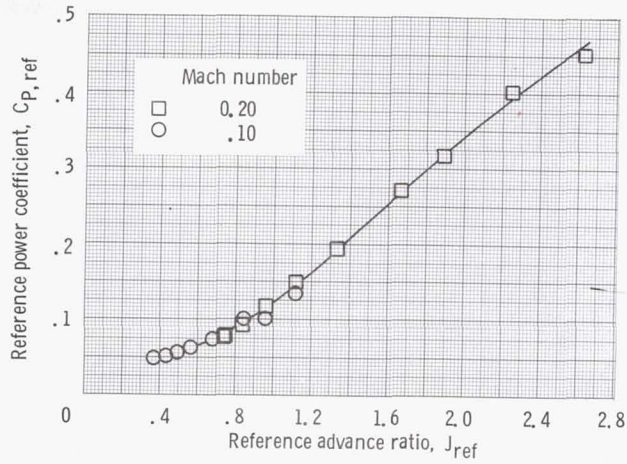
Figure 41. - SR-3 propeller efficiency comparison between two different wind tunnels and propeller test rigs at Mach 0. 20. Hamilton Standard data are from faired curves.

Figure 42. - SR-3 propeller power coefficient comparison between two different wind tunnels and propeller test rigs at Mach 0. 20. Hamilton Standard data are from faired curves.

Figure 43. - SR-3 reverse thrust power coefficient as function of advance ratio at Mach numbers of 0.10 and 0.20. Blade angle $\beta_{0.75R}$, -6.8^0.
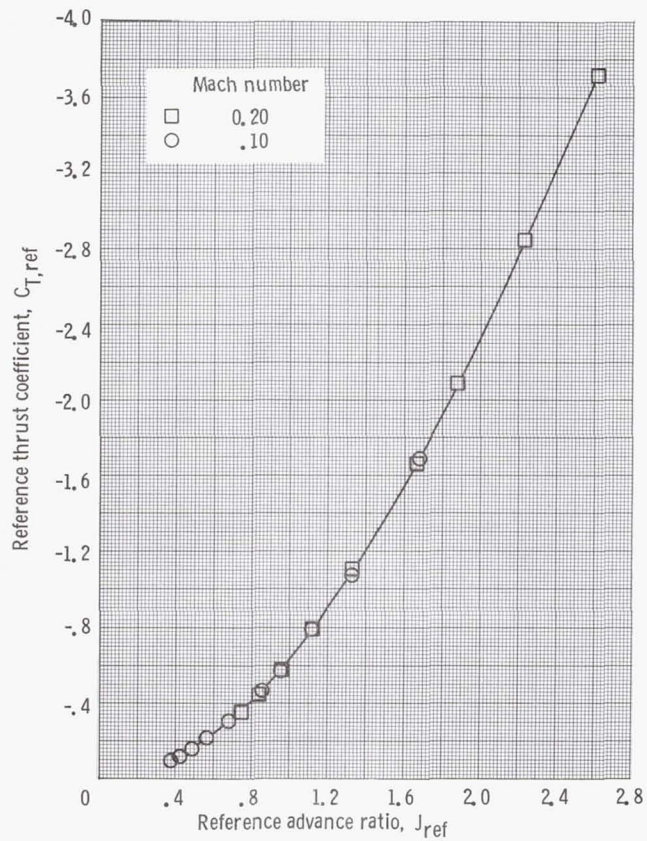

Figure 44. - SR-3 reverse thrust coefficient as function of advance ratio at Mach numbers of 0.10 and 0.20. Blade angle $\beta_{0.75R}$, -6.8^0.
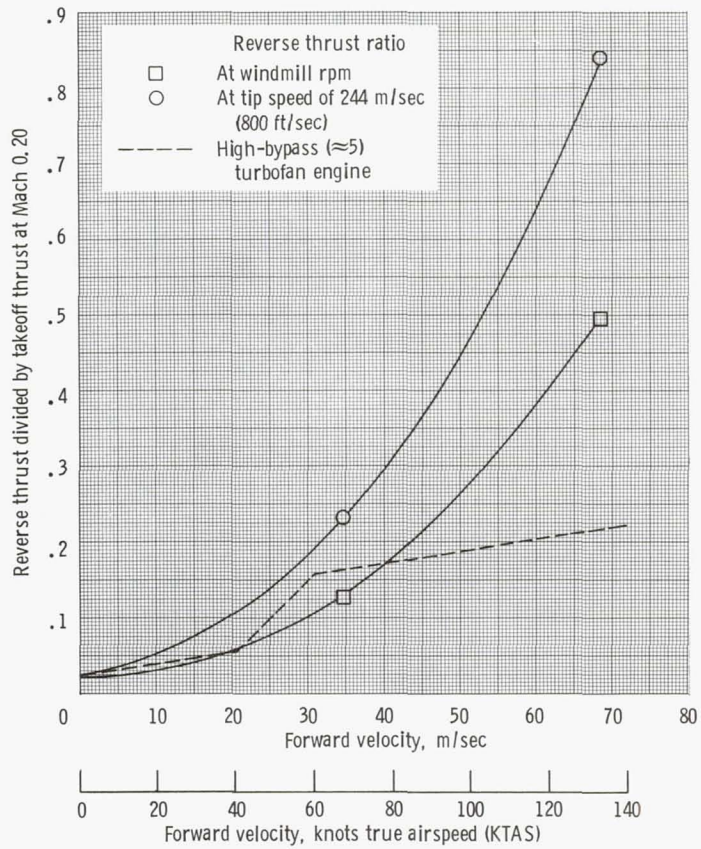
Figure 45. - The effect of forward velocity on the amount of reverse thrust produced relative to the amount of takeoff thrust produced at Mach 0.20. SR-3 propeller; blade angle $\beta_{0.75R}$, -6.8^0; takeoff thrust at Mach 0.20, 1427 N (321 lbf).
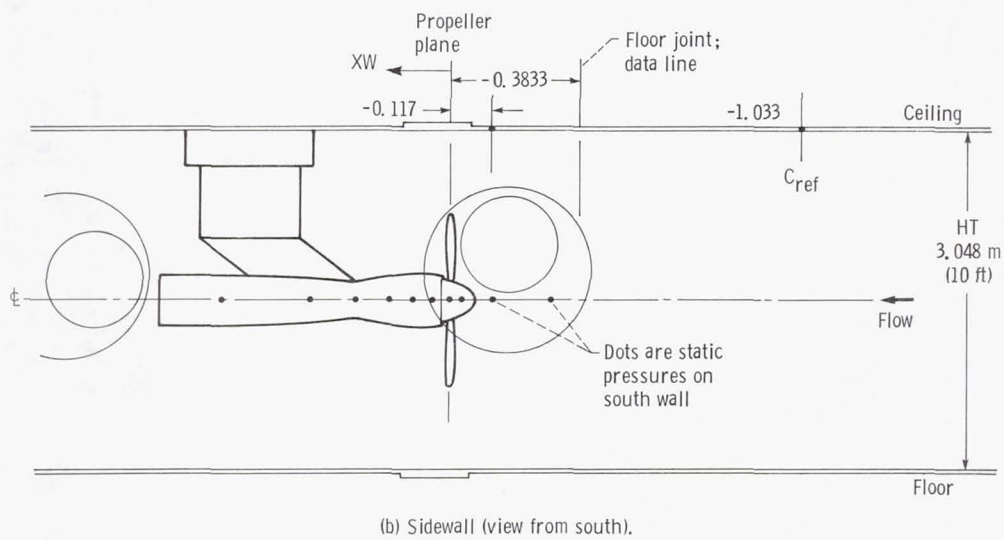
North

Propeller
Plane

P_o

C_{ref}

Ceiling plate

• Reference

HT
3.048 m
(10 ft)

0.1

0.15

Flow

Pressure taps

W_{10} W_9 W_8 W_7 W_6 W_4 W_2
W_5 W_3 W_1

South

Distance from
propeller plane
(XW) divided by
tunnel wall height
(HT) of 3.048 m
(10 ft) (XW/HT)

0.650   .400   .267   .167   .100   0   -.133   -.300
.050   -.033

Floor joint;
data line

(a) Ceiling (view from top).

Propeller
plane

XW

Floor joint;
data line

-0.3833

-0.117

-1.033

Ceiling

C_{ref}

HT
3.048 m
(10 ft)

Flow

Dots are static
pressures on
south wall

Floor

(b) Sidewall (view from south).
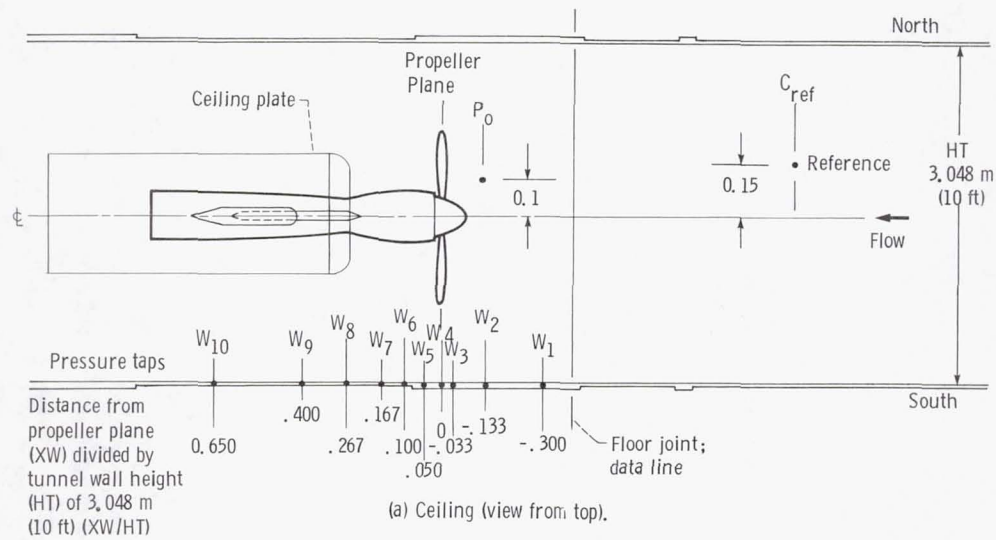
Figure 46. - Static-pressure locations for propeller-tunnel interference test. Propeller plane normalized by the tunnel wall height HT = 3.048 m (10 ft).
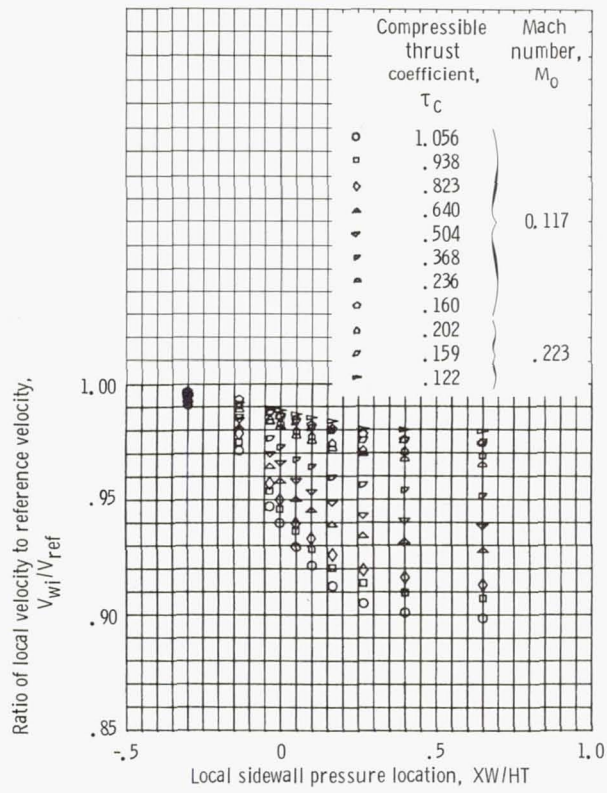
Figure 47. - Axial variation of measured velocity change for two free-stream Mach numbers and various thrust levels.
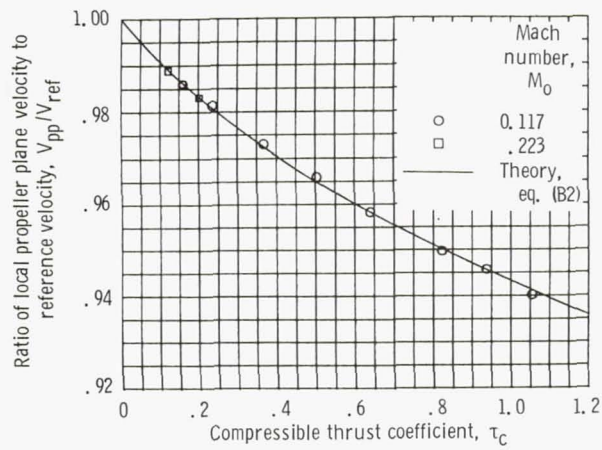

Figure 48. - Variation of measured and theoretical velocity change with thrust coefficient.
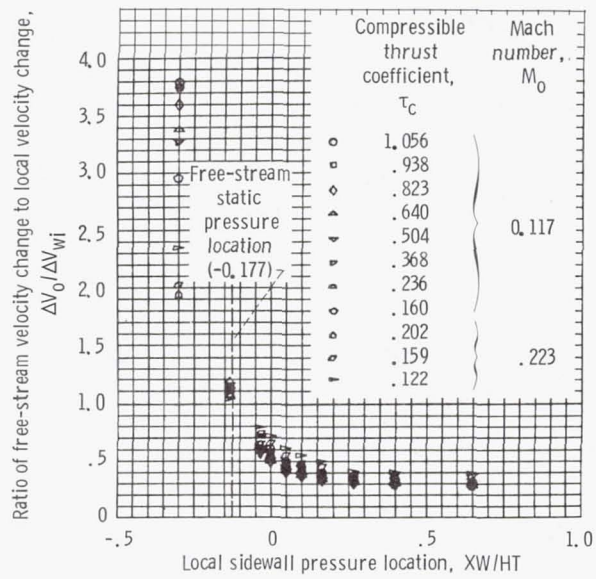
Figure 49. - Axial variation of ratio of free-stream change
to local change of velocity for two free-stream Mach
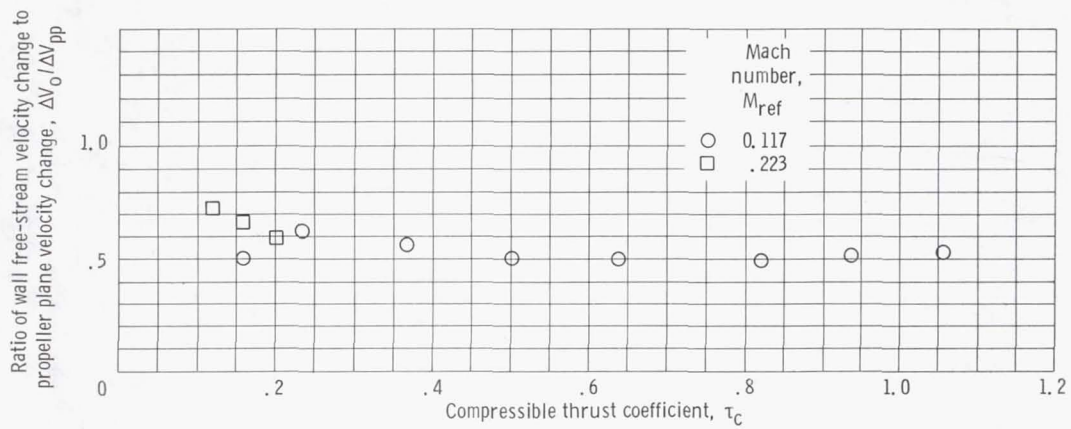numbers and various thrust levels.

Figure 50. - Variation of ratio of wall free-stream velocity change to propeller plane velocity change as function
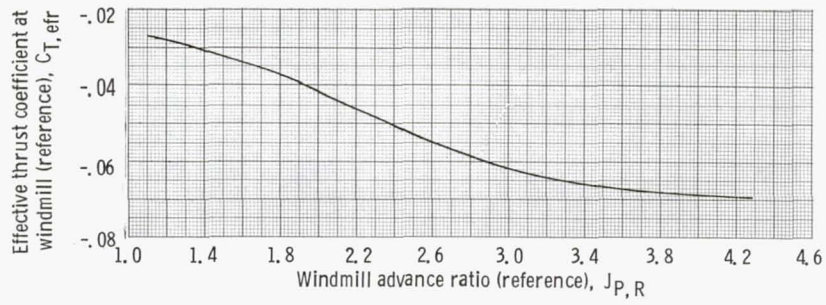of compressible thrust coefficient.

Figure 51. - SR-2 reference windmill thrust coefficient as function of reference windmill advance ratio for performance calculations at Mach numbers 0. 10 to 0. 34.
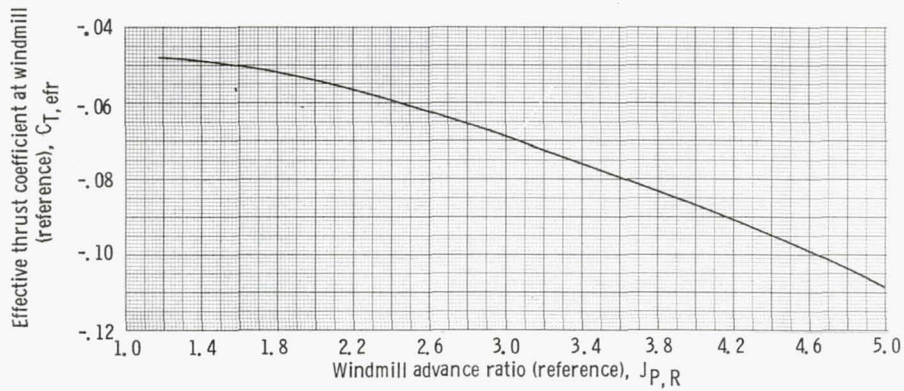

Figure 52. - SR-3 reference windmill thrust coefficient as function of reference windmill advance ratio for performance calculations at Mach numbers 0. 10 to 0. 34.
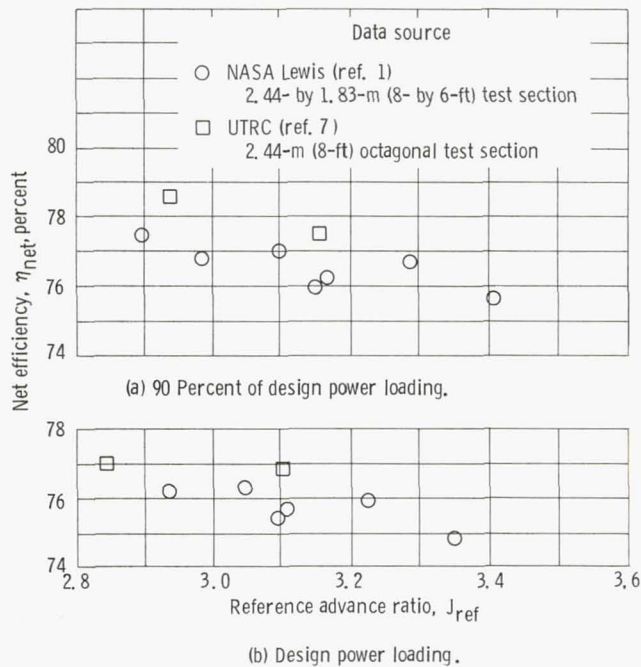

(a) 90 Percent of design power loading.

(b) Design power loading.

Figure 53. - Performance comparison for data from two wind tunnels for SR-1 propfan with 30^0-sweep and conic spinner. Free-stream Mach number of 0. 8.

1. Report No.	2. Government Accession No.	3. Recipient's Catalog No.
NASA TM-87030		

4. Title and Subtitle	5. Report Date
Wind-Tunnel Results of Advanced High-Speed Propellers at Takeoff, Climb, and Landing Mach Numbers	November 1985
	6. Performing Organization Code
	505-45-48

7. Author(s)	8. Performing Organization Report No.
George L. Stefko and Robert J. Jeracki	E-2417
	10. Work Unit No.

9. Performing Organization Name and Address	11. Contract or Grant No.
National Aeronautics and Space Administration Lewis Research Center Cleveland, Ohio 44135	
	13. Type of Report and Period Covered

12. Sponsoring Agency Name and Address	Technical Memorandum
National Aeronautics and Space Administration Washington, D.C. 20546	14. Sponsoring Agency Code

15. Supplementary Notes

16. Abstract

Low-speed wind-tunnel performance tests of two advanced propellers have been completed at the NASA Lewis Research Center as part of the NASA Advanced Turbo-prop Program. The 62.2-cm- (24.5 in-) diameter adjustable-pitch models were tested at Mach numbers typical of takeoff, initial climbout, and landing speeds (i.e., from Mach 0.10 to 0.34) at zero angle of attack in the NASA Lewis 10- by 10-Foot Supersonic Wind Tunnel. Both models had eight blades and a cruise-design-point operating condition of Mach 0.80, a 10.668-km (35 000-ft) I.S.A. altitude, a 243.8-m/s (800-ft/sec) tip speed, and a high-power loading of 301 kW/m^2 (37.5 shp/ft^2). Each model had its own integrally designed area-ruled spinner, but used the same specially contoured nacelle. These features reduced blade-section Mach numbers and relieved blade-root choking at the cruise condition. No adverse or unusual low-speed operating conditions were found during the test with either the straight-blade SR-2 or the 45°-swept SR-3 propeller. Typical net efficiencies of the straight and 45°-swept propellers were 50.2 and 54.9 percent, respectively, at a takeoff condition of Mach 0.20 and 53.7 and 59.1 percent, respectively, at a climb condition of Mach 0.34.

17. Key Words (Suggested by Author(s))	18. Distribution Statement
Propellers Advanced turboprop Energy efficient Prop-fan	LIMITED DISTRIBUTION Until February 1989 STAR Category 02

19. Security Classif. (of this report)	20. Security Classif. (of this page)	21. No. of pages	22. Price*
Unclassified	Unclassified		